

# The evolution of the radio luminosity function of group galaxies in COSMOS

E. Vardoulaki<sup>1,2\*</sup>, G. Gozaliasl<sup>3,4</sup>, A. Finoguenov<sup>4</sup>, M. Novak<sup>5</sup>, H. G. Khosroshahi<sup>6</sup>

<sup>1</sup> IAASARS, National Observatory of Athens, Lofos Nymfon, 11852 Athens, Greece

<sup>2</sup> Thüringer Landessternwarte, Sternwarte 5, 07778 Tautenburg, Germany

<sup>3</sup> Department of Computer Science, Aalto University, PO Box 15400, Espoo, FI-00076, Finland

<sup>4</sup> Department of Physics, University of Helsinki, P. O. Box 64, FI-00014, Helsinki, Finland

<sup>5</sup> Max-Planck-Institut für Astronomie, Königstuhl 17, D-69117, Heidelberg, Germany

<sup>6</sup> School of Astronomy, Institute for Research in Fundamental Sciences (IPM), P.O. Box 1956836613, Tehran, Iran

Received ; accepted 02/05/2024

## ABSTRACT

To understand the role of the galaxy group environment on galaxy evolution, we present a study of radio luminosity functions (RLFs) of group galaxies based on the Karl G. Jansky Very Large Array-COSMOS 3 GHz Large Project. The radio-selected sample of 7826 COSMOS galaxies with robust optical/near-infrared counterparts, excellent photometric coverage, and the COSMOS X-ray galaxy groups ( $M_{200c} > 10^{13.5} M_{\odot}$ ) enables us to construct the RLF of group galaxies (GGs) and their contribution to the total RLF since  $z \sim 2.3$ . Using the Markov chain Monte Carlo algorithm, we fit a redshift-dependent pure luminosity evolution model and a linear and power-law model to the luminosity functions. We compare it with past RLF studies from VLA-COSMOS on individual populations of radio-selected star-forming galaxies (SFGs) and galaxies hosting active galactic nuclei (AGN). These populations are classified based on the presence or absence of a radio excess concerning the star-formation rates derived from the infrared emission. We find that the density of radio galaxies in groups is low compared to the field at  $z \sim 2$  down to  $z \sim 1.25$ , followed by a sharp increase at  $z \sim 1$  by a factor of 6, and then a smooth decline towards low redshifts. This trend is caused by both decrease in the volume abundance of massive groups at high- $z$  and the changes in the halo occupation of radio AGN, which are found by other studies to reside at smaller halo mass groups. This indicates that the bulk of high- $z$   $\log_{10}(M_{200c}/M_{\odot}) > 13.5$  groups must have been forming recently, and so the cooling has not been established as yet. The slope of the GG RLF is flatter compared to the field, with excess at high radio luminosities. The evolution in the GG RLF is driven mainly by satellite galaxies in groups. At  $z \sim 1$ , the peak in the RLF, coinciding with a known overdensity in COSMOS, is mainly driven by AGN, while at  $z > 1$  SFGs dominate the RLF of group galaxies. A drop in occurrence of AGN in groups at  $z > 1$  by a factor of 6, manifests an important detail on the processes governing galaxy evolution.

**Key words.** galaxies: evolution – radio continuum: galaxies

## 1. Introduction

The properties and evolution of galaxies are known to be strongly linked to their external environment. Massive halos are found to play a key role in galaxy evolution. At low redshifts, it has been found that clusters of galaxies are mostly dominated by early-type galaxies composed of old stellar populations, while low-density environments host typically late-type galaxies with younger and bluer stars, producing the star-formation (SF) - density - distance to cluster centers relations and affecting the morphology of galaxies (e.g., Oemler 1974; Dressler 1980). We expect that galaxies in dense regions experience various physical processes such as tidal forces, mergers, high-speed interactions, harassment, and gas stripping, which in turn contribute to dramatic morphological changes and quenching of star formation (e.g. Larson 1980; Byrd & Valtonen 1990). However, these physical processes' precise timing and relative importance are not yet well understood.

The environmental processes which affect galaxy evolution could directly or indirectly influence the accretion onto the central black hole in galaxies, notably those with a stellar bulge (Magorrian et al. 1998). Both local and large-scale processes

which may affect cluster galaxies also have the potential to affect the gas distribution in the galaxies and hence may trigger or suppress active galactic nuclei (AGN) activity.

Apart from the role of galaxy group and cluster environment on radio emission of the brightest galaxy of the group, Khosroshahi et al. (2017) suggested that the radio luminosity of the brightest group galaxy (BGG) also depends on the group dynamics, in a way that BGGs in groups with a relaxed/virialised morphology are less radio luminous than the BGG with the same stellar mass but in an evolving group. This was supported numerically by a semi-analytic approach (Raouf et al. 2018), where they predicted the radio power for the first time. However, the numerical models cannot be constrained without an observational constraint reaching high redshift.

Many radio studies (Best et al. 2002; Barr et al. 2003; Miller & Owen 2003; Reddy & Yun 2004) showed an increase in radio-loud AGN activity in galaxy clusters, at a range of redshifts, and in both relaxed and merging systems. The radio emission (< 30 GHz) in galaxies is dominated by synchrotron radiation from accelerating relativistic electrons, with a fraction of free-free emission (e.g., Sadler et al. 1989; Condon 1992; Clemens et al. 2008; Tabatabaei et al. 2017). The feedback from supernovae explosions in star-forming galaxies (SFGs) and that from the growth

\* email: elenivard@gmail.com

of the central supermassive black hole (SMBH) in AGN are two main sources of acceleration of cosmic electrons.

To use radio emission as a proxy for measuring star formation rates (SFRs) or AGN feedback, it is important to estimate which process dominates the radio emission: star formation processes or SMBH accretion. We follow the method demonstrated in (Delvecchio et al. 2017) who measured the radio excess compared to the total star-formation-based infrared (IR) emission. Objects which exhibit radio excess above what is expected from star formation alone, as calculated from their infrared emission, are deemed AGN, and the rest are SFGs. These populations contribute different percentages to the energy budget. In the radio, this is quantified by calculating the radio luminosity function (RLF). Novak et al. (2018) studied the 3 GHz VLA-COSMOS RLF and calculated the relative contributions to the RLF from the AGN and SFG populations down to submicrojansky levels. AGN and SFGs contribute differently to the RLF, where AGN are known to dominate the bright part of the RLF, and SFGs dominate the faint. In particular, 90% of the population at the faint end ( $< 0.1\text{mJy}$ ) is linked to SFGs. In clusters of galaxies, Yuan et al. (2016) who studied the RLF of brightest cluster galaxies (BCGs) up to  $z = 0.45$  found no evolution, and a dominant population of AGN, as most of their BCGs are associated with AGN. Branchesi et al. (2006) compared clusters at  $0.6 < z < 0.8$  to the local Abell clusters and found very different RLFs. These studies target populations dominated by AGN and thus probe the high end of the radio luminosity function. The question arises, how much do smaller mass environments, those of groups of galaxies, and their members contribute to the observed radio source population.

In this paper we investigate the population of galaxies inside X-ray galaxy groups in the COSMOS field (Gozaliasl et al. 2019) to quantify their contribution to the RLF at 3 GHz VLA-COSMOS (Novak et al. 2018; Smolčić et al. 2017b). Section 2 describes the X-ray and radio data used throughout this work. Section 3 focuses on methods for deriving the RLF and its evolution through cosmic time. In Section 4, we present and discuss the results on the RLF of group galaxies and calculate their contribution to the total RLF at 3 GHz. We further separate the galaxies to BGGs and satellites (SGs). We also use the radio excess parameter and the presence of jets/lobes to disentangle AGN and SFGs in the radio and provide the relative contributions of these populations to the group galaxies (GG) RLF and the total RLF. This is presented in Section 5. Finally, in Section 6, we provide a summary. The tables with the analysis results can be found in the Appendix.

We assume flat concordance Lambda Cold Dark Matter ( $\Lambda$ CDM) cosmology defined with a Hubble constant of  $H_0 = 70 \text{ km s}^{-1} \text{ Mpc}^{-1}$ , dark energy density of  $\Omega_\Lambda = 0.7$ , and matter density of  $\Omega_m = 0.3$ . For the radio spectral energy distribution, we assume a simple power law described as  $S_\nu \propto \nu^{-\alpha}$ , where  $S_\nu$  is the flux density at frequency  $\nu$  and  $\alpha$  is the spectral index. If not explicitly stated otherwise,  $\alpha = 0.7$  is assumed.

## 2. The Data

The Cosmic Evolution Survey (COSMOS) is a deep multi-band survey covering a  $2 \text{ deg}^2$  area, thus offering a comprehensive data set to study the evolution of galaxies and galaxy systems. The full definition and survey goals can be found in Scoville et al. (2007). The sample selection for this study is described below.

### 2.1. Radio selected galaxies

We used radio-selected samples of galaxies cross-matched with multi-wavelength optical/near-infrared (NIR) and value-added catalogues in the COSMOS field. The radio data have been selected from the VLA-COSMOS 3 GHz Large Project (Smolčić et al. 2017b), with a median sensitivity of  $2.3 \mu\text{Jy beam}^{-1}$  and resolution of 0.75 arcsec. The cross-correlation of the radio and multiwavelength sources can be found in Smolčić et al. (2017a). Only sources within the COSMOS2015 catalogue (Laigle et al. 2016) or with *i*-band counterparts have been given the availability of reliable redshift measurements. The COSMOS2015 catalogue contains the high-quality multiwavelength photometry of  $\sim 800\,000$  sources across more than 30 bands from near-ultraviolet (NUV) to near-infrared (NIR) through several surveys and legacy programs (see Laigle et al. 2016, for detailed description).

### 2.2. X-ray galaxy groups catalogue

Finoguenov et al. (2007) and George et al. (2011) presented primary catalogs of the X-ray galaxy groups in COSMOS. These catalogs combined the available *Chandra* and *XMM-Newton* data (with improvements in the photometric datasets) used to identify galaxy groups, with secure identification reaching out to  $z \sim 1.0$ . On completion of the visionary *Chandra* program (Elvis et al. 2009; Civano et al. 2016), high-resolution imaging across the full COSMOS field became available. Furthermore, more reliable photometric data provided a robust identification of galaxy groups at a higher redshift, thus resulting in a revised catalogue of extended X-ray sources in COSMOS (Gozaliasl et al. 2019), which was obtained by combining both the *Chandra* and *XMM-Newton* data for the COSMOS field.

The COSMOS galaxy group catalogue that we use in this study relies on a combination of an updated version of the initial group catalogs with 183 groups and a new catalogue of 73 groups described in Gozaliasl et al. (2019) and Gozaliasl et al. (in preparation), which combines data of all X-ray observations from *Chandra* and *XMM-Newton* in the 0.5-2 keV band, with robust group identification up to  $z \sim 2.0$ . It reaches an X-ray limit of  $3 \times 10^{-16} \text{ erg cm}^{-2} \text{ s}^{-1}$  in the range 0.5-2 keV and contains groups with  $M_{200c} = 8 \times 10^{12} - 3 \times 10^{14} M_\odot$ .

Group halo mass is the total mass (commonly called  $M_{200c}$ ) which was determined using the scaling relation  $L_X - M_{200c}$  with weak lensing mass calibration as presented by Leauthaud et al. (2010). The radius of the group  $R_{200}$  is defined as the radius enclosing  $M_{200c}$  with a mean overdensity of  $\Delta \sim 200$  times the critical background density. Gozaliasl et al. (2019) discussed the mass completeness of the group sample given the surface brightness limitation of the X-ray dataset. Over the redshift range  $0.5 < z < 1.2$ , the evolution of the group mass limit is weak and lies within the observational uncertainties, being around  $\log(M_{\text{group}}/M_\odot) \sim 13.38$  at  $z \sim 0.5$  and  $\log(M_{\text{group}}/M_\odot) \sim 13.5$  at  $z > 0.5$ .

The redshift of the group is the redshift of the peak of the galaxy distribution within the group radius while slicing the lightcone with a redshift step of 0.05. In most cases, this redshift determination is strengthened by the presence of spectroscopic galaxies redshifts. The brightest group galaxy (BGG) is detected from the COSMOS2015 photometry as being the most massive galaxy within  $R_{200}$ , with a redshift that matches that of the hosting group (Gozaliasl et al. 2019). More than  $\sim 80\%$  of the BGGs have robust spectroscopic redshifts. The center of groups from the X-ray emission is determined with an accuracy of  $\sim 5''$ , us-

ing the smaller scale emission detected by *Chandra* data. The BGGs do not always locate at the peak of the X-ray center emission. As described in Gozaliasl et al. (2019), the off-central BGG probably resides in groups more likely to have experienced a recent halo merger. The rest of the group galaxies (GGs) are called satellites (SGs).

A quality flag has been assigned to groups depending on the robustness of the extraction and the potential availability of spectroscopic redshift (Gozaliasl et al. 2019). In our study, we keep only the groups with flags 1, 2, and 3. We considered only groups with BGG galaxies more massive than  $\log M_*/M_\odot = 10$ . We refer the reader to Gozaliasl et al. (2019) for further information on identifying groups. Within the virial radius of these groups, the above selection criteria resulted in a total of 306 objects distributed in the galaxy groups. In Fig. 1 we present the data for the group galaxies used in our analysis. The spectroscopic redshifts are available for 35% of our sources, and the median accuracy of the photometric redshifts is  $\Delta z/(1+z_{\text{spec}}) = 0.007$  (Laigle et al. 2016).

### 2.3. Sample of group galaxies used in this analysis

To analyse the radio luminosity function of group galaxies in COSMOS, we cross-match the galaxy group catalogue and the 3 GHz VLA-COSMOS data (Smolčić et al. 2017b) within a radius of  $0.8''$ . We furthermore use the 3 GHz VLA-COSMOS data presented in Novak et al. (2018), who constructed RLFs up to  $z \sim 5.5$ , to compare to the total RLF in COSMOS up to  $z \sim 2.3$ . Additionally, Novak et al. (2018) separated objects in SFGs and AGN, following the radio excess prescription of Delvecchio et al. (2017). This method is based on the excess radio emission expected from star formation alone. Delvecchio et al. (2017) fitted the infrared spectral energy distribution of radio sources at 3 GHz VLA-COSMOS and calculated the contribution of the 3 GHz VLA-COSMOS radio sources to the radio luminosity by applying a conservative cut. Galaxies that exhibit an excess in radio emission above  $3\sigma$  from what is expected from SF alone were deemed AGN, with the rest being SFGs. This method was used to separate the Novak et al. (2018) sample, which we use here for comparison, in SFGs and AGN. Finally, Novak et al. (2018) described possible biases and uncertainties associated with the data sample selection, and thus we refer the reader to this reference.

## 3. Methods and analysis

We describe the process of calculating the RLF for galaxies in groups in COSMOS (Gozaliasl et al. 2019) using the VLA-COSMOS 3 GHz data. We applied a cut in group mass  $M_{200c} > 10^{13.5} M_\odot$ , to account for a difference in the limiting mass of the group catalogue with redshift (Sec. 2.2). This cut is demonstrated at the bottom frame of Fig. 1. We further separate group galaxies in BGGs and SGs. We compare the RLF of the population of SFGs and AGN at 3 GHz VLA-COSMOS in the same redshift bins to the total RLF calculated from the 3 GHz data (Novak et al. 2017; Smolčić et al. 2017b). We fit linear and power-law models to the RLFs of GGs and compare them to the total RLF to obtain the contribution of GGs to the total RLF at 3 GHz VLA-COSMOS, something that has not been shown before in COSMOS.

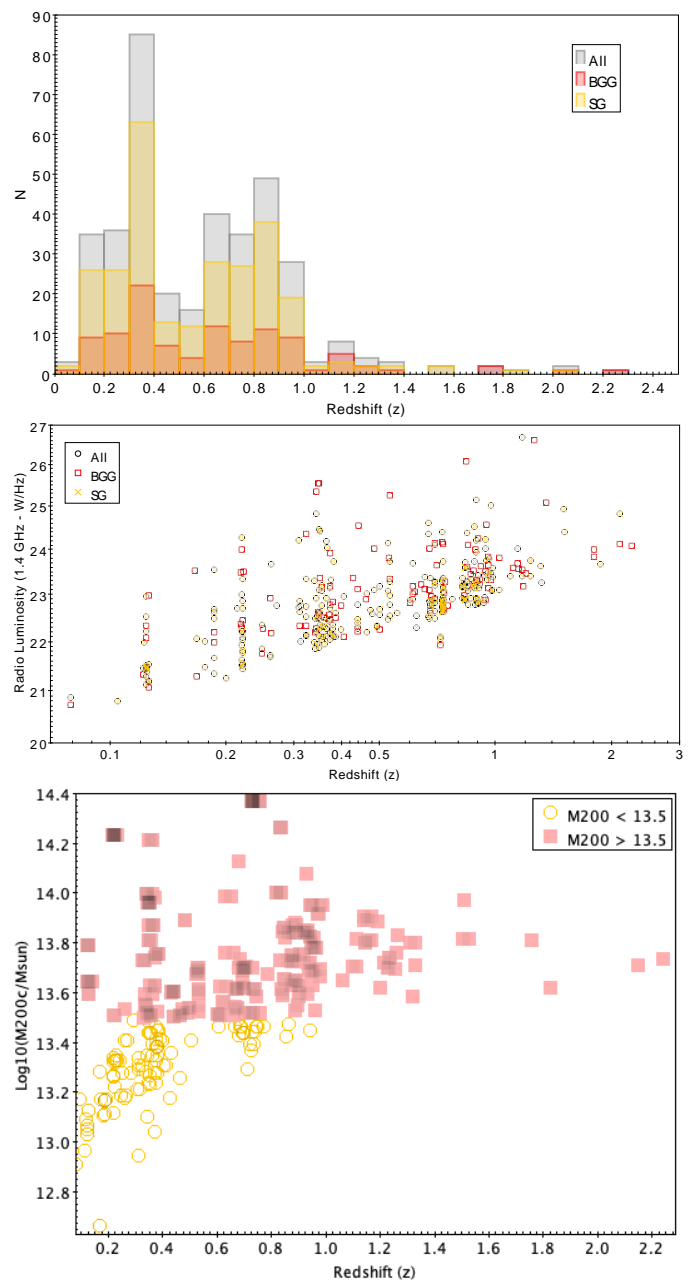


**Fig. 1.** Top: Number of sources per redshift. The bin size is 0.1. Middle: Radio luminosity at 1.4 GHz versus redshift. The redshift plotted is the one of the galaxy groups. The radio luminosity is calculated from the 1.4 GHz flux density for the redshift of the object. Black represents all group galaxies, red is for BGGs, and yellow is for SGs (see Sec. 2 for clarification on the classification). Bottom: Halo mass versus redshift. Pink filled squares denote  $\log_{10}(M_{200}/M_\odot) > 13.5$  and yellow open circles  $\log_{10}(M_{200}/M_\odot) < 13.5$ , which we refer to as  $\log_{10}(M_{200}/M_\odot) \approx 13.3$  in the rest of the paper. The divide shows our adopted halo mass cut to account for sample completeness (Sec. 2.2).

### 3.1. Measuring the radio luminosity function

To obtain the total RLFs, for GGs, SFGs, and AGN, we followed the method adopted by Novak et al. (2017) (see their Sec. 3.1). They computed the maximum observable volume  $V_{\text{max}}$  for each source (Schmidt 1968) and simultaneously applied completeness corrections that take into account the non-uniform *rms* noise and the resolution bias (see Sec. 3.1 in Novak et al. 2017). Then the

RLF is

$$\Phi(L, z) = \frac{1}{\Delta \log L} \sum_{i=1}^N \frac{1}{V_{max,i}} \quad (1)$$

where  $L$  is the rest-frame luminosity at 1.4 GHz, derived using the radio spectral index of a source calculated between 1.4 GHz (Schinnerer et al. 2010) and 3 GHz (Smolčić et al. 2017b), and  $\Delta \log L$  is the width of the luminosity bin. The radio spectral index should remain unchanged between frequencies and is only available for a quarter of the 3 GHz VLA-COSMOS sample. For the rest of the sources detected only at 3 GHz, we assumed  $\alpha = 0.7$ . The latter corresponds to the average spectral index of the entire 3 GHz population (see Sec. 4 in Smolčić et al. 2017b).  $V_{max}$  is the maximum observable volume given by

$$V_{max,i} = \sum_{z=z_{min}}^{z_{max}} [V(z + \Delta z) - V(z)] C(z), \quad (2)$$

where the sum starts at  $z_{min}$  and adds co-moving spherical shells of volume  $\Delta V = V(z + \Delta z) - V(z)$  in small redshift steps  $\Delta z = 0.01$  until  $z_{max}$ .  $C(z)$  is the redshift-dependent geometrical and statistical correction factor. This takes into account sample incompleteness. For a thorough description of the biases, see Section 6.4 in Novak et al. (2017). The correction factor is given by

$$C(z) = \frac{A_{obs}}{41253 \text{ deg}^2} \times C_{radio}(S_{3\text{GHz}}(z)) \times C_{opt}(z), \quad (3)$$

where  $A_{obs} = 1.77 \text{ deg}^2$  is the effective unflagged area observed in the optical to NIR wavelengths,  $C_{radio}$  is the completeness of the radio catalogue as a function of the flux density  $S_{3\text{GHz}}$ , and  $C_{opt}$  is the completeness owing to radio sources without assigned optical-NIR counterpart. Completeness corrections are shown in Smolčić et al. (2017b) in their Fig. 16 and Table 2, and in Novak et al. (2017) in their Fig. 2.

The redshift bins are large enough not to be affected severely by photometric redshift uncertainty and follow the selection of Novak et al. (2017) to allow comparisons. Luminosity bins in each redshift bin span the data's observed luminosity range. To eliminate possible issues due to poorer sampling, the lowest luminosity ranges from the faintest observed source to the  $5\sigma$  detection threshold at the upper redshift limit (corresponding to  $5 \times 2.3 \mu\text{Jy beam}^{-1}$  at 3 GHz). The reported luminosity for each RLF is the median luminosity of the sources within the bin. The RLFs for all group galaxies are shown in Figs 2 and 3 (black points) and are also listed in Table A.2. The RLFs for the BGGs and SGs are also shown in Figs 2 and 3 (red squares/yellow stars) and are listed in Tables A.3 and A.4, respectively. The  $z$  bins in Figs 2 and 3 are split in two halo mass  $M_{200c}$  bins, above and below  $10^{13.5} M_{\odot}$ , and for our further analysis, we use the values above. We note that at  $1.6 < z < 2.3$  we do not have SGs above our halo-mass cut ( $M_{200c} > 10^{13.5} M_{\odot}$ ). This is related to limits in the radio power that are probed at those redshifts, leading to low statistics and scarcity of less massive groups. As discussed in Novak et al. (2018), there is only a 5-10% loss of completeness on the optical/NIR counterparts above  $z \sim 2$ .

### 3.2. The total RLF at 3 GHz VLA-COSMOS

We use the total RLF derived from the SFG and AGN populations at 3 GHz VLA-COSMOS (Novak et al. 2017, 2018;

Smolčić et al. 2017c) to compare to the RLF values derived for the group galaxies in COSMOS. The RLF of the SFG and AGN populations are calculated similarly for the same redshift bins as described above and for the same area coverage as the galaxy groups in COSMOS. To fit the RLF, two models are used in literature (e.g., Condon 1984; Sadler et al. 2002; Gruppioni et al. 2013), the pure luminosity evolution (PLE) and the pure density evolution (PDE). The RLF is fitted, assuming its shape remains unchanged at all observed cosmic times. Only the position of the turnover and normalisation can change with redshift. This corresponds to the translation of the local LF in the  $\log L - \log \Phi$  plane (Condon 1984) and can be divided into pure luminosity evolution (horizontal shift) and pure density evolution (vertical shift).

To describe an RLF across cosmic time, the local RLF is evolved in luminosity or density, or both (e.g. Condon 1984). This is parametrised (Novak et al. 2018) using two free parameters for density evolution ( $\alpha_D, \beta_D$ ), and two for luminosity evolution ( $\alpha_L, \beta_L$ ) to obtain

$$\Phi(L, z, \alpha_L, \beta_L, \alpha_D, \beta_D) = (1+z)^{\alpha_D + z\beta_D} \times \Phi_0 \left( \frac{L}{(1+z)^{\alpha_L + z\beta_L}} \right), \quad (4)$$

where  $\Phi_0$  is the local RLF. Since the shape and evolution of the RLF depend on the galaxy population type, Novak et al. (2017) used a power-law plus log-normal shape of the local RLF for SFGs. They used the combined data from Condon et al. (2002), Best et al. (2005) and Mauch & Sadler (2007) to obtain the best fit for the local value

$$\Phi_0^{\text{SF}}(L) = \Phi_{\star} \left( \frac{L}{L_{\star}} \right)^{1-\alpha} \exp \left[ -\frac{1}{2\sigma^2} \log^2 \left( 1 + \frac{L}{L_{\star}} \right) \right], \quad (5)$$

where  $\Phi_{\star} = 3.55 \times 10^{-3} \text{ Mpc}^{-3} \text{ dex}^{-1}$ ,  $L_{\star} = 1.85 \times 10^{21} \text{ W Hz}^{-1}$ ,  $\alpha = 1.22$ , and  $\sigma = 0.63$ .

It was noted by Novak et al. (2017) that the PDE of SF galaxies would push the densities to very high numbers, thus making them inconsistent with the observed cosmic star formation rate densities. This is a consequence of the fact that our data can constrain only the bright log-normal part of the SF RLF. For AGN, it was shown by Smolčić et al. (2017c) that the PDE and PLE models are similar, mostly because the shape of the RLF does not deviate strongly from a simple power law at the observed luminosities. Considering the above reasoning, while also trying to keep the parameter space degeneracy to a minimum, we decided to use only the PLE for our analysis. Thus we adopt the approach of Novak et al. (2018), who fitted the total RLF for SFG and AGN populations by constructing a four-parameter redshift-dependent pure luminosity evolution model with two parameters for the SFG and AGN populations of the form:

$$\begin{aligned} \Phi(L, z, \alpha_L^{\text{SF}}, \beta_L^{\text{SF}}, \alpha_L^{\text{AGN}}, \beta_L^{\text{AGN}}) &= \\ &= \Phi_0^{\text{SF}} \left( \frac{L}{(1+z)^{\alpha_L^{\text{SF}} + z\beta_L^{\text{SF}}}} \right) + \Phi_0^{\text{AGN}} \left( \frac{L}{(1+z)^{\alpha_L^{\text{AGN}} + z\beta_L^{\text{AGN}}}} \right), \end{aligned} \quad (6)$$

where  $\Phi_0^{\text{SF}}$  is the local RLF for SFGs as in Eq. 5, and for the non-local Universe is a function of the quantity in the parenthesis,  $L/(1+z)^{\alpha_L^{\text{SF}} + z\beta_L^{\text{SF}}}$ .  $\Phi_0^{\text{AGN}}$  is the local RLF for AGN of the form

$$\Phi_0^{\text{AGN}}(L) = \frac{\Phi_{\star}}{(L_{\star}/L)^{\alpha} + (L_{\star}/L)^{\beta}}, \quad (7)$$

where  $\Phi_{\star} = \frac{1}{0.4} 10^{-5.5} \text{ Mpc}^{-3} \text{ dex}^{-1}$ ,  $L_{\star} = 10^{24.59} \text{ W Hz}^{-1}$ ,  $\alpha = -1.27$ , and  $\beta = -0.49$  (Smolčić et al. 2017c; Mauch &

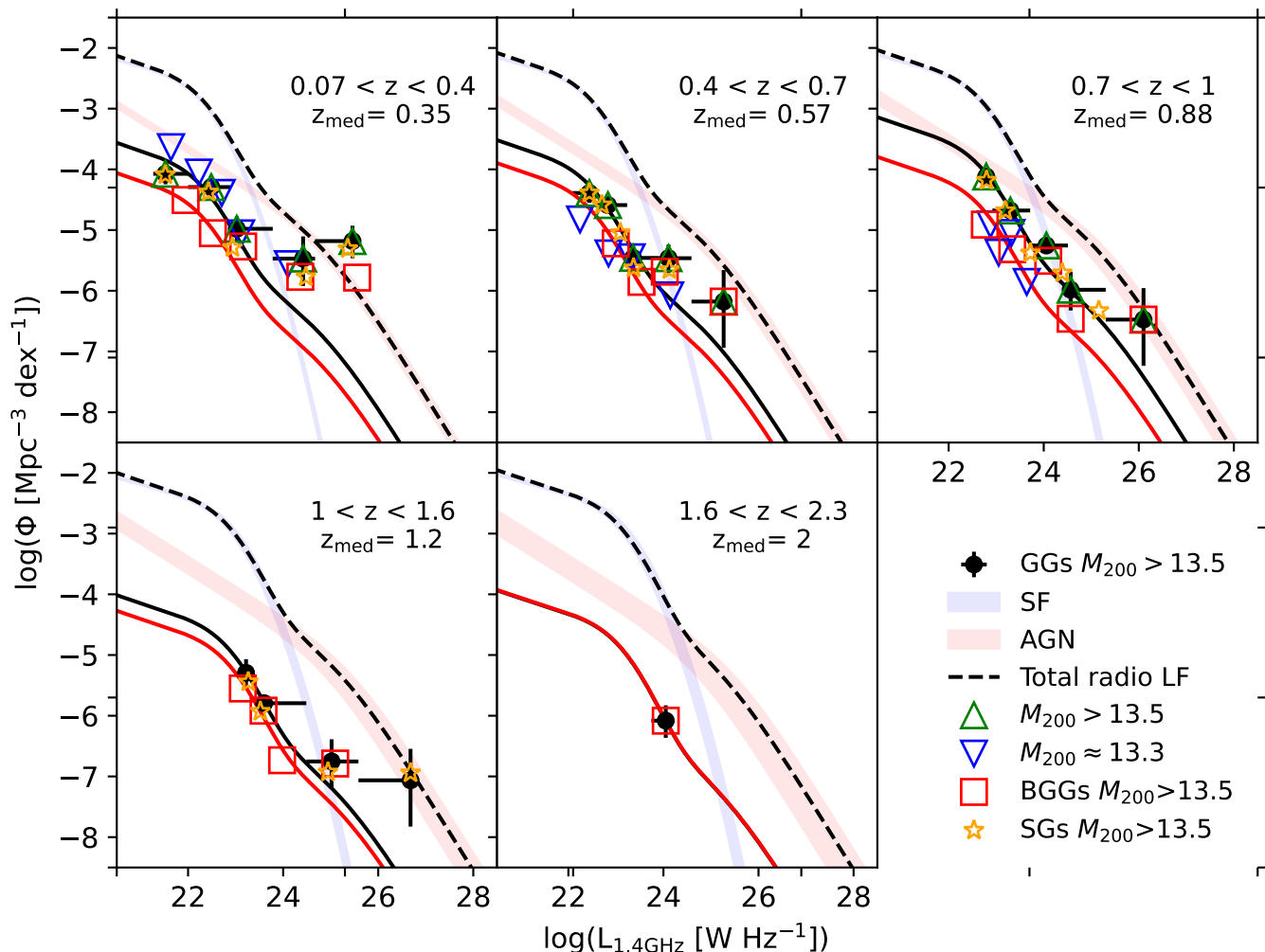


**Fig. 2.** Total radio luminosity functions of galaxies in groups. Black points indicate the RLFs for group galaxies derived using the  $V_{\max}$  method (see Section 3.1). Red squares and yellow stars mark the brightest group galaxies and satellites, respectively. The blue and red shaded areas show the  $\pm 3\sigma$  ranges of the best-fit evolution for the individual SFG and AGN populations, respectively (outlined in Section 3.2). The black dashed line is the fit to the total RLF at 3 GHz VLA-COSMOS (Novak et al. 2017; Smolčić et al. 2017c). For the  $z < 1$  sub-samples ( $z < 0.4$ ), the halos have been split into massive ( $M_{200c} > 10^{13.5} M_{\odot}$ ) and low-mass halos ( $M_{200c} \approx 10^{13.3} M_{\odot}$ ); the latter are shown for completion but not used in the analysis. For the rest of the redshift bins, all samples have  $M_{200c} > 10^{13.5} M_{\odot}$ . A halo mass cut,  $M_{200c} > 10^{13.5} M_{\odot}$ , was applied to the GGs, BGGs, and SGs. The black solid line is the scaled fit to the group galaxies RLF, and the red solid line is the scaled fit for BGGs, as explained in Section 3.3.1. The scaled fit can be found in Fig. 2, and we do not show it here for SGs for clarity. The black line for the scaled fit for GGs in the last redshift bin is hidden by the red line for BGGs, because there are no SGs in that bin.

Sadler 2007), and for the non-local Universe is a function of the quantity  $L/(1+z)^{\alpha_L^{\text{AGN}} + z\beta_L^{\text{AGN}}}$ .

Novak et al. (2018) used the Markov chain Monte Carlo (MCMC) algorithm, available in the Python package `EMCEE` (Foreman-Mackey et al. 2013), to perform a multi-variate fit to the data. The redshift dependence of the total evolution parameter  $\alpha + z \cdot \beta$  (see Eq. 6) is necessary to describe the observations at all redshifts. The best fit values, based on the results of Novak et al. (2018), for SFGs are  $\alpha_L^{\text{SF}} = 3.16$  and  $\beta_L^{\text{SF}} = -0.32$ , and for AGN are  $\alpha_L^{\text{AGN}} = 2.88$  and  $\beta_L^{\text{AGN}} = -0.84$ . The  $\alpha_L$  and  $\beta_L$  values for both SFGs and AGN are valid for  $z < 5.5$  and within the redshift range of our sample of group galaxies. We use these values to plot the fit to the RLF for SFGs and AGN in Fig. 3, shown in blue and red lines, respectively. The total RLF (including all SFG and AGN), is shown as a dashed black line in Fig. 3.

### 3.3. Fitting the RLF of group galaxies and comparing to the total 3 GHz RLF

Fitting the GG RLF is not a simple task. Performing an MCMC fit to the GG data with four free parameters ( $\alpha_{\text{SF}}, \beta_{\text{SF}}, \alpha_{\text{AGN}}$  and  $\beta_{\text{AGN}}$ ), in a similar way it was done in Novak et al. (2018) is proven problematic and the MCMC does not converge. Below we investigate whether the functional form of the RLF, as presented above can fit the GG RLF.

#### 3.3.1. Scaled fit

We scale the total 3 GHz RLF to fit the GG RLF using MCMC. The resulting GG RLF is shown in Fig. 2. There is a large deviation in the RLF values of GGs compared to the scaled fit, especially above luminosities  $10^{26} \text{W Hz}^{-1}$ . We perform a  $\chi^2$  test for the goodness of the fit between the GG values and the predicted scaled fit. The results are shown in Table A.9 in the Appendix.

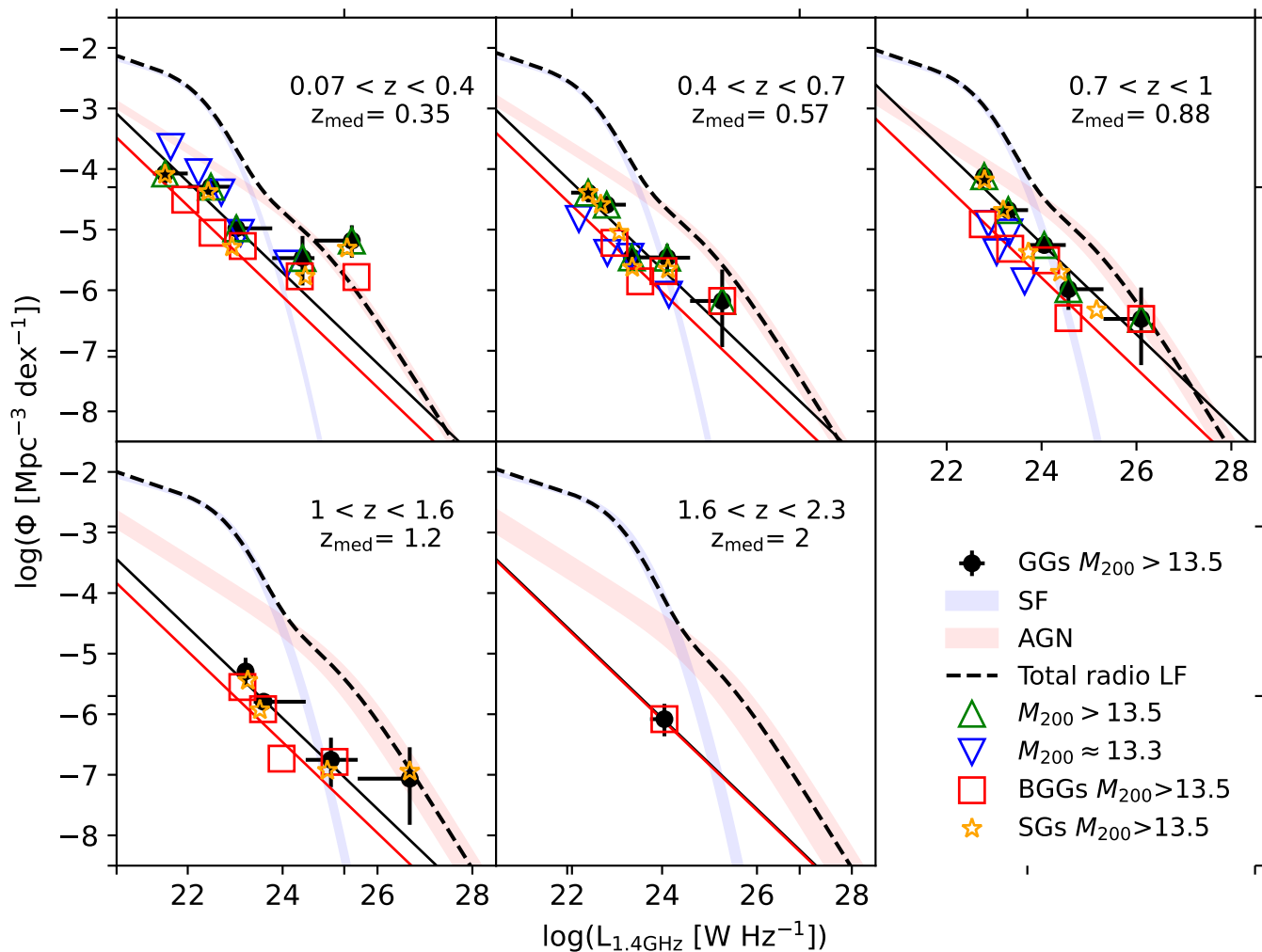


**Fig. 3.** Same as Fig. 2: Total radio luminosity functions of galaxies in groups. Black points indicate the RLFs for group galaxies derived using the  $V_{\max}$  method (see Section 3.1). Red squares and yellow stars mark the brightest group galaxies and satellites, respectively. The blue and red shaded areas show the  $\pm 3\sigma$  ranges of the best-fit evolution for the individual SFG and AGN populations, respectively (outlined in Section 3.2). The black dashed line is the fit to the total RLF at 3 GHz VLA-COSMOS (Novak et al. 2017; Smolčić et al. 2017c). For the  $z < 1$  sub-samples ( $z < 0.4$ ), the halos have been split into massive ( $M_{200c} > 10^{13.5} M_{\odot}$ ) and low-mass halos ( $M_{200c} \approx 10^{13.3} M_{\odot}$ ); the latter are shown for completion but not used in the analysis. For the rest of the redshift bins, all samples have  $M_{200c} > 10^{13.5} M_{\odot}$ . A halo mass cut,  $M_{200c} > 10^{13.5} M_{\odot}$ , was applied to the GGs, BGGs, and SGs. The black solid line is the fit to the group galaxies RLF, and the red solid line is the best fit for BGGs, as explained in Section 3.3.2. We do not show the best fit for SGs for clarity. The black line for the linear regression fit for GGs in the last redshift bin is hidden by the red line for BGGs, because there are no SGs in that bin.

The  $\chi^2$  is large for most redshift bins, suggesting the model is not a good fit to the data. Additionally, we plot the ratio between data and model (see Fig. 4). It is evident that for the redshift bins with  $z_{\text{med}} = 0.35$  and  $1.2$  the model under-fits the data in the high luminosity bins by up to  $\sim 2$  orders of magnitude, suggesting that the functional form of the RLF does not work well in the case of group galaxies. Hence, we explore an alternative method for fitting the GG RLF.

### 3.3.2. Power-law fit

We fit a power-law (linear regression fit in log-log) to the radio luminosity function of the group galaxies, and separately of the BGGs and SGs, from redshifts 0.07 to 2.3 of the form

$$y = \Phi_{\star} / (L_{\star}^{\gamma}) * L^{\gamma}, \quad (8)$$

where  $L_{\star}$  is arbitrarily chosen to be  $10^{24} \text{ W Hz}^{-1}$ , and  $\Phi_{\star}$  is the density at  $L_{\star}$ . Table A.5 shows the results for each fit. The best-

fit model for the GGs is shown in Fig. 3, where we also compare the radio luminosity function of group galaxies to the total radio luminosity function of radio galaxies in the 3GHz VLA-COSMOS survey and the radio luminosity function of AGN and the star-forming population. We also present the linear regression fit for BGGs, but exclude the one for SGs for clarity. The radio emission due to the star formation over-weighs that from the AGN in lower redshifts, i.e., at  $z < 1$ , except at high radio luminosity bins where the AGN contribution dominates. This behaviour has been described in Novak et al. (2017); Smolčić et al. (2017b) and agrees with other surveys. Adopting a fit similar to the total RLF, similar to that used in Novak et al. (2018), provides a very poor fit to the GG data, particularly in the high luminosity bins. Similarly, allowing for both luminosity and  $\Phi_{\star}$  to be free parameters resulted in the slope fit being dominated by two points with the smallest error. These tell us the GGs do not necessarily follow the shape of the total 3GHz RLF, particu-

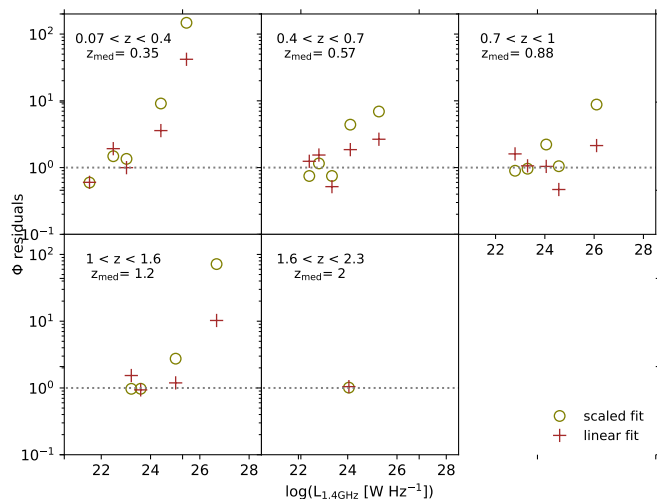


**Fig. 4.** Ratio of  $\Phi$  GG RLF data points in the adopted luminosity range and in each redshift bin, and the corresponding model value. Olive open circles denote the scaled fit method (Sec. 3.3.1) and brown crosses denote the linear regression fit method (Sec. 3.3.2). The dotted grey line shows a perfect agreement between data and model.

larly at high luminosities, where we see increased radio activity of GG member galaxies.

### 3.3.3. Methods comparison

To investigate which method fits best the GG RLF, we compare the predicted to the real values. As mentioned earlier, we performed a  $\chi^2$  test for the goodness of the fit between the GG values and the predicted (Table A.9). The test yields similar results for both methods, where the linear regression fit gives slightly better results, but neither of the models is good fit to the data.

Furthermore, we visually inspect the RLF grid plots in Figs 2 & 3. Both methods provide fairly good fits to the data. Should we use these fitted lines to predict a value, it would not necessarily agree with the observed values in some areas of the parameter space. In particular, as seen in Fig. 2 for the scaled RLF, the scaled RLF does not fit well the GGs above radio luminosity  $10^{25}$  W/Hz in all redshift bins, i.e. the part that can be dominated by AGN contribution (based on the 3GHz RLF). In Fig. 3, for the power-law RLF, we also see the fit is not good for GGs above radio luminosity  $10^{25}$  W/Hz but mainly in the redshift bins  $z \sim 0.35$  and  $z \sim 1.2$ . From the ratio between data and model in Fig. 4 we see that the linear regression fit deviates less, on average, than the scaled fit from the observational data at all luminosities and redshifts.

To sum up, the  $\chi^2$  test suggests neither of the fitting methods fits the data well. By visual inspection and from the ratio between data and model (Fig. 4) we see that we under-fit the GG RLF when using either of the two fitting methods for radio luminosities above  $10^{25}$  W  $\text{Hz}^{-1}$  in the redshift bins  $z_{\text{med}} = 0.35$  and 1.2. Below this value, there is a good rough agreement, with marginally better fits for the power-law RLF. The ratio between data and model in Fig. 4 aids us in selecting a method, i.e. the power-law, linear regression fit. Thus, for the remainder of this analysis we use the power-law fit method, but also present results of the scaled method for completeness (see Table A.6).

### 3.3.4. GG contribution to the total RLF

We calculate fractions obtained by the different methods we examined, the fraction of GG RLF to the total RLF if we apply the power-law linear regression fit (Sec. 3.3.2) and the fraction of GG RLF to the total RLF if we apply the scaled RLF (Sec. 3.3.1).

To quantify the contribution of the RLF of group galaxies to the total RLF of the 3 GHz population, we divide the power-law RLF of GGs, assuming a fixed slope of  $\gamma = -0.75$ , with the total RLF from the 3 GHz sample for each redshift bin. This gives the fractional contribution of group galaxies to the total RLF. In the top panel of Fig. 5, we plot the fraction with respect to the radio luminosity at 1.4 GHz up to  $10^{25}$  W  $\text{Hz}^{-1}$ . The reason for that is the RLF of 3 GHz VLA-COSMOS observations is not well constrained above that luminosity (Novak et al. 2018). Furthermore, we should consider that our model might be a good representation of the universe at  $L > 10^{25}$  W  $\text{Hz}^{-1}$ , and the COSMOS is not suited for low- $z$  studies due to the small volume coverage at low redshifts. Because of the different total RLF shapes per redshift bin, there is a bump in the curve, as expected. Using a fixed slope of  $\gamma = -0.75$  does not impact our calculations as the value is within the errors for the fitted  $\gamma$  values presented in Table A.5.

We also calculate the RLF of all massive galaxies with  $M_* > 10^{11.2} M_{\odot}$ , which are 3 GHz sources, and compare it to the total RLF. This fraction is shown in the middle panel of Fig. 5. We see an increase in the contribution to the total RLF at  $z_{\text{med}} = 0.3$ , and at higher redshifts similar to that of GGs. The choice of this stellar mass cut, as a comparison, was motivated by the study of Smolčić et al. (2017c) in order to select massive galaxies across all redshifts. We will discuss this further in the next section.

The bottom panel of Fig. 5 presents fractions using the scaled fit method presented in Sec. 3.3.1. The fraction is the same across the adopted luminosity range, as expected for a scaled fit.

In Fig. 6 we plot the radio luminosity function and the fraction, for the scaled and power-law fits, in relation to redshift for the GGs, BGGs, and SGs, and discuss this in the following section.

## 4. Evolution of the RLF in galaxy groups

The top panel of Fig. 5 shows that the contribution of GGs to the total RLF increases from  $z \sim 2$  to 0.07, and in particular for objects above radio luminosities at  $10^{23}$  W  $\text{Hz}^{-1}$ . This picture suggests an evolutionary scenario for the RLF of galaxy groups. We investigate this further by plotting in Fig. 6 the RLF of GGs, BGGs, and SGs (left panel), and their relative contribution to the total 3 GHz RLF as a function of redshift (right panel). The GG RLF has a low value at  $\sim 2$  down to  $z \sim 1.25$  followed by a sharp increase in the GG RLF at  $z \sim 1$  by a factor of 6, and then a smooth decline, mimicking a mild evolution by a factor of 2. This is an interesting trend, which is not observed in the total RLF. As seen by the normalisation value of the total  $\Phi_*$  for a fixed radio luminosity at  $10^{24}$  W  $\text{Hz}^{-1}$ , shown with cyan, galaxies in the 3 GHz sample display a decrease in their RLF with redshift across all redshifts, while the RLF of GGs increases at  $z \sim 1$  (left panel of Fig. 6); the peak at  $z_{\text{med}} \sim 0.9$  coincides with known overdensities in the COSMOS field. Interestingly, Smolčić et al. (2017c) show that a similar trend can be reproduced with galaxies. In their Fig. 1, they present a slight increase in the median values of  $M_*$  in their radio excess sample up to redshift  $z = 1$ , and depletion of massive galaxies above  $z > 1$ , which we also see in the X-ray groups. We observed this at a median value  $\sim 10^{11.2} M_{\odot}$ . At the middle panel of Fig. 5 we see that massive galaxies above  $10^{11.2} M_{\odot}$  contribute a large fraction

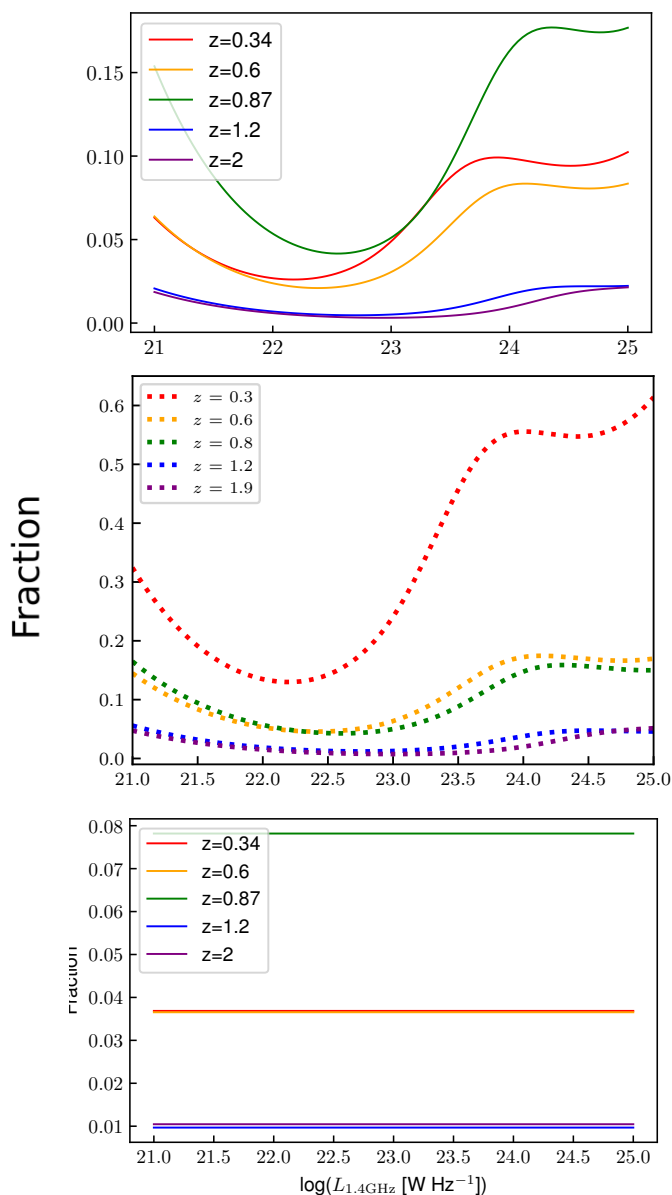


**Fig. 5.** Top: Fraction for group galaxies showing their contribution to the total 3 GHz radio luminosity function at different epochs using the power-law, linear regression fit method presented in Sec. 3.3.2 vs. radio luminosity at 1.4 GHz. Colours represent different redshift bins. Middle: Same as above, but for all massive galaxies ( $M_* > 10^{11.2} M_\odot$ ) with radio emission at 3 GHz (Smolčić et al. 2017a; Laigle et al. 2016). Bottom: Fraction using the scaled fit method presented in Sec. 3.3.1. A halo mass cut above  $10^{13.5} M_\odot$  was applied to all plots.

to the total 3 GHz RLF below  $z < 1$ . This suggests that not all massive galaxies are in groups, but those that are, remain radio active (Fig. 5). The GG contribution to the RLF has a nearly flat but slightly enhanced behaviour below  $z < 0.75$ , while the GGs RLF does not exhibit a large contribution of radio emission at the lowest redshift bin like the massive galaxies RLF does. This suggests those massive galaxies are either in the field or occupy halo masses below our adopted cut at  $\log_{10}(M_{200c}/M_\odot) > 13.5$ .

The RLF of SGs dominates the RLF of group galaxies up to redshift of  $z_{\text{med}} \sim 1.2$ , with overdensities below  $z = 1$  (Fig. 6–

Right). The fraction for the linear regression fit method is a range of values that correspond to the adopted luminosity range (see also Fig. 5), plotted as violin plots. Both fractions follow the mild evolutionary trend we observe on the left panel. Scoville et al. (2013) studied the large-scale structure (LSS) in COSMOS and also report a statistically significant overdensity at  $z = 0.93$ . Additionally, the strongest density peaks, where we have massive clusters in COSMOS, are at redshifts 0.37, 0.73, and 0.83. Our  $0.4 < z < 0.7$  bin misses LSS on both ends. Above  $z \sim 2$  we do not currently have a large-enough number of SGs to perform a robust analysis. This is likely to improve with future observations. The relative contribution of the SGs to the RLF of group galaxies is higher by a factor of 2 than that of BGGs below  $z \sim 1$ . Additionally, BGGs contribute a small amount to the RLF of GGs, as seen by the left panel of Fig. 6, despite being the most massive galaxies of the group. This is a very interesting result highlighting the importance of identifying the member group galaxies within a group and the need for high sensitivity and high-resolution observations.

For reference we have split the redshift bins into low and high halo mass objects. Objects with group masses below  $10^{13.5} M_\odot$  contribute significantly to the lowest redshift bins and are linked to SGs, but this contribution is not taken into account in our analysis, to ensure our sample is complete (see Sec. 2). The low halo mass points (Table A.5 & Fig. 3) show a faster turnover as we do not expect to detect many low mass, high luminosity objects.

Yuan et al. (2016), who studied brightest cluster galaxies (BCGs), found that RLFs of 7138 BCGs in the range  $0.05 < z < 0.45$  do not show significant evolution with redshift. This no-evolution pattern of BCGs agrees with our results for BGGs in COSMOS. At the left panel of Fig. 6, we see that the RLF of BGGs fluctuates slightly with redshift, but it is the RLF of satellites that drives the redshift evolution.

Novak et al. (2018) discuss possible biases which could affect the calculations. These include the assumed shape of the radio SED to be a power law and the radio excess criterion to be too conservative and thus excluding low-luminosity AGN from the sample. We refer the reader to their discussion (see their Section 3.4). Furthermore, Novak et al. (2018) discuss possible biases that affect the RLF of the high luminosity bin, i.e., bright radio but faint in the near-infrared sources ( $K = 24.5$  mag). We have constrained our sample to halo masses above  $10^{13.5} M_\odot$ , to perform an unbiased analysis. Incidentally, after the halo-mass cut, the remaining group galaxies in our sample are brighter than  $K = 24.5$  mag.

In summary, we observe a nearly flat but slightly enhanced behavior of the contribution of X-ray galaxy groups to the 3 GHz RLF up to  $z \sim 0.75$ , driven by SGs and AGN (see Sec. 5) in GGs, followed by an increase and then a sharp drop. This agrees with past studies of the COSMOS field, and in particular with the study of Hale et al. (2018), who in their Fig. 10 showed that the AGN bias starts to deviate from values close to  $5 \times 10^{13} M_\odot$  at  $z < 1$  towards  $1 \times 10^{13} M_\odot$  at  $z > 1$ . This explains the sharp drop we observe at  $z > 1$ , since we are probing halo masses  $> 10^{13.5} M_\odot$  (see bottom panel of Fig. 1).

## 5. The AGN and SFG contribution to the GG RLF

The group galaxy population has a mixture of contributions from AGN and SFGs. To explore how much these populations contribute to the GG RLF, we cross-correlate the X-ray galaxy group catalogue with the sample of Vardoulaki et al. (2021), which is a value-added catalogue at 3 GHz VLA-COSMOS, and includes

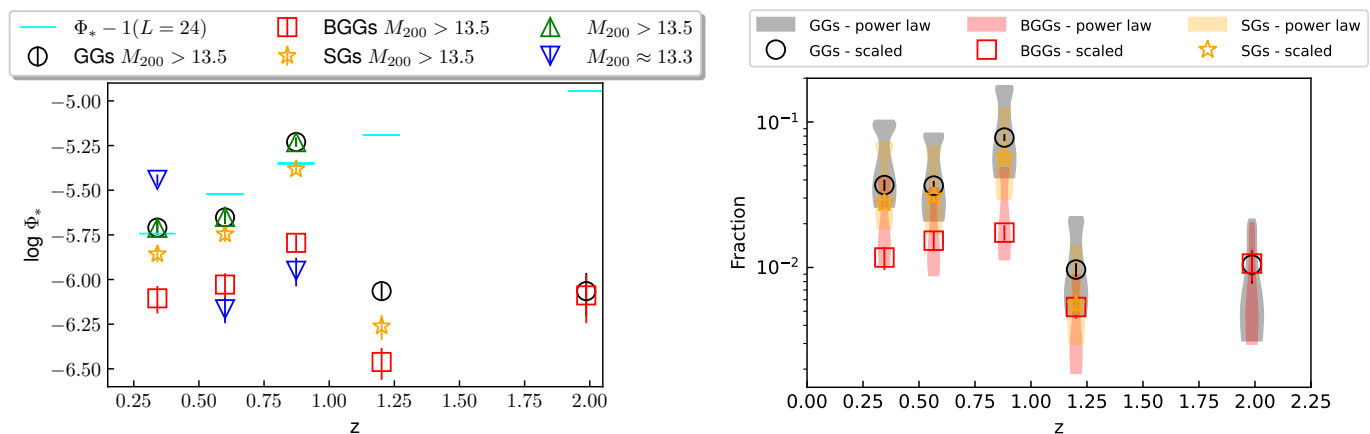


**Fig. 6.** Left: Radio luminosity function vs. redshift for the group galaxies (black circles), brightest group galaxies BGGs (red squares), and satellite galaxies SGs (yellow stars). Cyan lines show the  $\Phi_*$  values at  $\log_{10}(L_{1.4\text{GHz}}/W \text{ Hz}^{-1}) = 24$  for each redshift bin; these values were placed a dex lower for presentation reasons. The values plotted here are reported in Table A.5 for  $\gamma = -0.75$ . Right: The relative contribution of GGs to the total radio luminosity, as described in Sec. 3.3.1 for the scaled fit (open symbols) and in Sec. 3.3.2 for the power-law, linear regression fit (violin plots), vs. redshift. The values in the violin plots show the distribution of fractions along our adopted luminosity range. Black circles denote GGs, red squares denote BGGs, and yellow stars denote SGs. A halo mass cut,  $\log_{10}(M_{200c}/M_{\odot}) > 13.5$ , was applied.

**Table 1.** The AGN and SFGs inside X-ray galaxy groups. Data from (Vardoulaki et al. 2021), cross-correlated with the X-ray galaxy group catalogue (Gozaliasl et al. 2019, and in prep.).

Number of sources	AGN	SFGs
total 3 GHz VLA-COSMOS	1948	7232
same area & $z$ as X-ray groups	1038	6452
X-ray group members	138	240
BGGs	67	47
SGs	71	193

130 FR-type radio sources (FRI, FRII; Fanaroff & Riley 1974, and hybrids FRI/FRII) and 1818 jet-less compact radio AGN (COM AGN), as well as 7232 SFGs (see Table 5). Radio AGN in the Smolčić et al. (2017a) sample were selected on the basis of their radio excess, as mentioned above. This criterion, due to the  $3\sigma$  cut applied, excludes several FR-type radio AGN, which were identified in Vardoulaki et al. (2021) and classified as radio AGN because they exhibit jets/lobes. SFGs are objects which do not display radio excess.

To quantify the contribution of these populations separately to the group RLF and to the total RLF we calculate their RLF as described in Sec. 3, using the  $V_{\text{max}}$  method. All AGN and SFGs are in groups with halo masses  $M_{200c} > 10^{13.5} M_{\odot}$ . The results for the AGN and SFG populations inside galaxy groups are shown in Fig. 7, where we also plot the RLF of AGN and SFGs from the sample of Novak et al. (2018) as in Fig. 3 and the total RLF at 3 GHz. In order to compare the RLF of AGN and SFGs which are GGs and total RLF, we follow the analysis in Sec. 3.3.2. We fit a linear regression and normalise it to  $10^{24} \text{ W Hz}^{-1}$  by applying Eq. 8 for  $\gamma = -0.75$ . The results are shown in Fig. 7.

For completeness and to enable comparisons between the methods, we also present the scaled AGN and SFG parts of the total RLF to the GG data, and overplot it in Fig. 7. In Table 5 we give the scaling coefficients used in Fig. 2 at the five redshift

**Table 2.** Scaling coefficients for the functional form of the RLF (scaled fit) for the AGN and SFG populations.

	Redshift $z_{\text{med}}$				
	0.3	0.6	0.9	1.2	2
AGN	0.258	0.133	0.224	0.032	0.028
SFG	0.041	0.044	0.094	0.012	0.016

bins, separately for the AGN and SFG scaled fits. Visually, we see that the scaled RLF is not a good fit to the SFG at  $z < 0.4$  and to the AGN at  $z < 1.6$ , inside X-ray galaxy groups. We perform a  $\chi^2$  test for the AGN and SFGs, at all redshift bins and present the results in Table A.9. The results show that neither of the fitting methods fits the data well.

We further calculate and plot the fractional contribution of AGN and SFGs which lie inside groups to the total RLF at 3 GHz (Fig. 8), by replicating Fig. 5. The fraction was calculated by dividing the RLF of AGN and of SFGs inside galaxy groups by the total 3 GHz RLF. The fractions per redshift bin are curved lines due to the total RLF being curved. We find that there is a significant contribution from group AGN and SFGs at redshifts  $z < 1.6$ , and very little contribution above. We present the values for these fractions in Table 3. For completeness, we calculate the fractional contribution of the AGN and SFG RLF to the GG and total RLFs in the case where the scaled-fit method is used. The fractions are also presented in Table 5. In Fig. 8 we overplot the fraction of AGN and SFG RLF to the GG RLF, where both RLFs were calculated using the scaled-fit method. The respective lines follow the scaled AGN and SFG distributions, where AGN contribute more to the total RLF at higher luminosities, while SFGs dominate at lower luminosities. We stress that the scaled method for AGN and SFGs inside galaxy groups in COSMOS, and given the current dataset, is an approximation. It assumes the total 3GHz RLF fits the sub-populations of AGN and SFGs inside galaxy groups. The reason for using a scaled fit is the smaller numbers of objects in galaxy groups compared to the

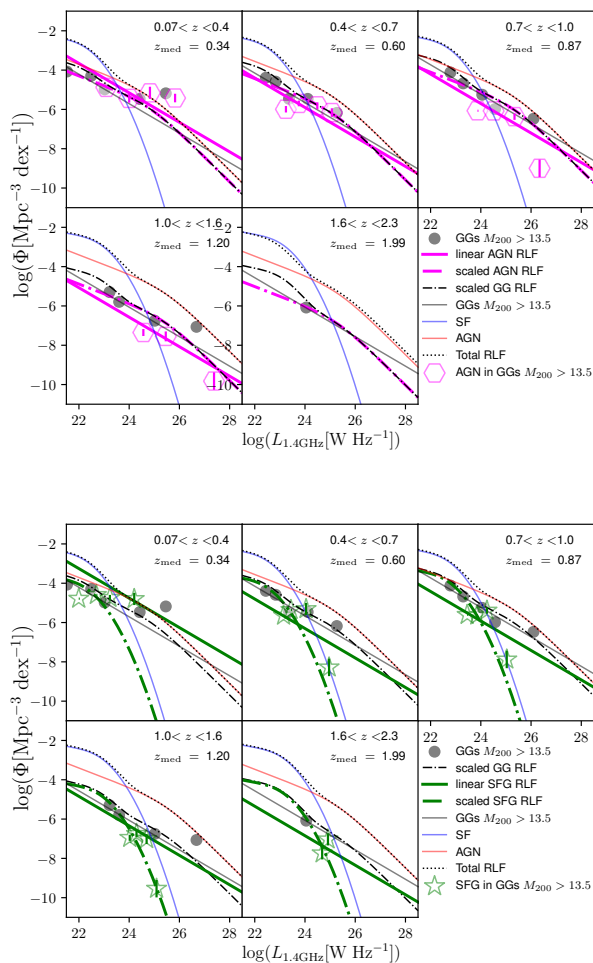


**Fig. 7.** Total radio luminosity functions of galaxies in groups, as in Figs 2 & 3, including RLFs for different populations: radio AGN inside galaxy groups as magenta hexagons (top) and SFGs inside galaxy groups as in Fig. 5), and for different populations (dotted lines): AGN (top; labelled AGN v tot) and SFGs (bottom; labelled SFG v tot). To compare to the GG sample, we normalise the fit to the AGN and SFGs inside groups to  $L_{1.4\text{GHz}} = 10^{24} \text{ W Hz}^{-1}$  and slope of  $\gamma = -0.75$ . For comparison, we show the GG sample (black circles for data, and a black solid line with a slope  $\gamma = -0.75$  for the fit). We also plot the scaled AGN and SFG RLF (dashed-dotted lines), as reference. The red solid line shows the RLF for all AGN, the blue solid line for all SFGs, and the dotted black line is the total RLF. A halo mass cut of  $M_{200c} > 10^{13.5} M_{\odot}$  was applied. We note, the green solid line at the last bin of the SFG sample is forced to go through the two green stars.

total 3GHz sample. Ideally, with a larger sample of AGN and SFGs inside groups, an MCMC can provide a good fit to the sub-populations. Our analysis suggests that the total 3GHz RLF is not a good fit for individual populations inside galaxy groups and that the picture is more complicated than that.

For the linear regression fit method we get a constant value across all luminosities in Fig. 8 because the divided fits are both linear. The contribution of AGN RLF to the GG RLF is significant at the redshift bin  $z_{\text{med}} = 0.6$  of around 56% and at  $z_{\text{med}} = 0.8$  with fraction around 33%, and dominates the GG RLF. The fraction in SFGs is around 20% for  $z_{\text{med}} = 0.6$  and  $z_{\text{med}} = 0.8$ , while at  $z_{\text{med}} = 1.2$  the SFGs are dominating the GG RLF, with a fraction of 52%. At  $z_{\text{med}} = 0.3$  we also see enhanced contribution in both AGN and SFGs compared to the GG RLF. This can be explained by the linear regression fit being normalised to

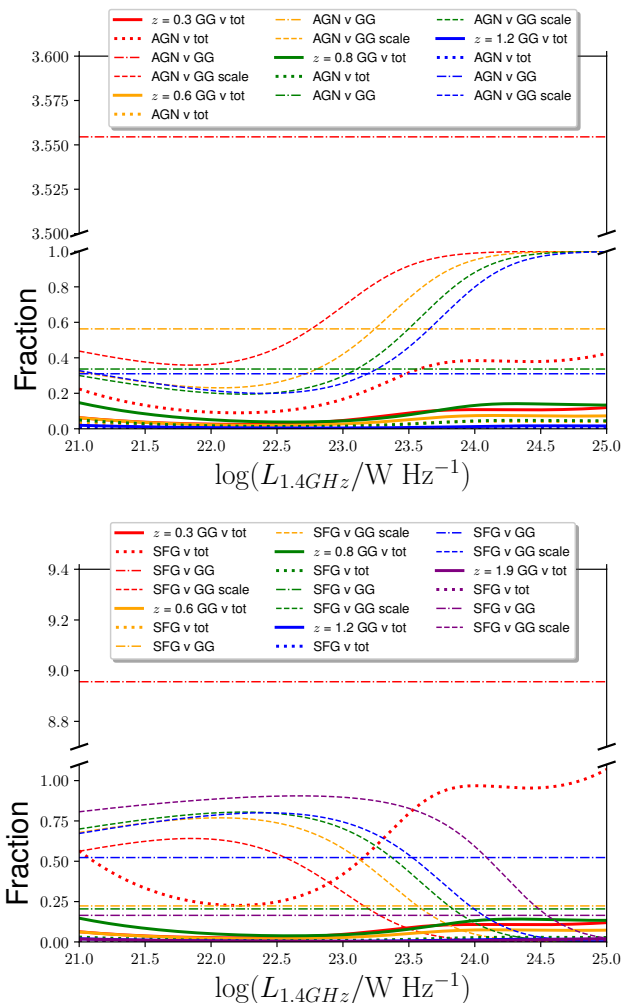


**Fig. 8.** Fractional contribution to the total radio luminosity function at different epochs vs radio luminosity at 1.4 GHz for GGs (solid lines labelled AGN v tot) and SFGs (bottom; labelled SFG v tot). Dotted-dashed lines show the fractional contribution of AGN (labelled AGN v GG) and SFG (labelled SFG v GG) to the GG RLF. For reference, we plot with dashed lines the fraction of scaled AGN RLF (top) and scaled SFG RLF (bottom) to scaled GG RLF

. Different colours represent different redshift bins as in Fig. 5.

A halo mass cut of  $M_{200c} > 10^{13.5} M_{\odot}$  was applied.

$10^{24} \text{ W Hz}^{-1}$  and forced to have a slope of  $\gamma = -0.75$ . For  $z > 1.6$  the contribution of SFGs to the GG RLF drops sharply and below 1%, while we do not have AGN above  $z > 1.6$ . These findings suggest that both AGN and SFGs contribute to the GG RLF, with the AGN contribution peaking around  $z \sim 1$ .

There are 67 AGN associated with BGGs and 71 with SGs, as shown in Table 5. For SFGs we get 47 BGGs and 193 SGs. Due to the small number of sources per bin, we cannot replicate Fig. 6 by splitting the AGN and SFGs RLF inside groups in BGGs and SGs and calculating their RLF. Fig. 6 suggests the evolution of the GG RLF is driven by satellites. Based on our results on from Fig. 8, at the  $z_{\text{med}} = 0.3$  redshift bin, the SG AGN or SFGs are responsible for the peak of the GG RLF, while at  $z_{\text{med}} = 0.8$  the increase is mainly driven by AGN.

How much of the AGN contribution to the GG RLF comes from extended radio emission, given the capabilities of the 3 GHz VLA-COSMOS survey, is not easy to estimate due to sam-

ple size limitations. From Table 5 we see that  $\sim 82\%$  of AGN inside galaxy groups are jet-less AGN. But in order to robustly answer this question we need to separate FRs and COM AGN inside groups and calculate their RLFs per redshift bin, as above, which we cannot do given the small number of FRs per redshift bin. To get an idea of how extended the FRs within the AGN sample are, we have a look at the linear projected sizes  $D$  of FRs in Vardoulaki et al. (2021). The sensitivity and resolution of the 3 GHz VLA-COSMOS survey are  $2.3 \mu\text{Jy}/\text{beam}$  and  $0''.75$ , respectively. This means that we are able to resolve and disentangle structures of  $\sim 6$  kpc at  $z \sim 2$ . The smallest FR reported in Vardoulaki et al. (2021) has  $D = 8.1$  kpc at  $z = 2.467$ , just above the resolution limit, and the smallest edge-brightened FR has  $D = 24.3$  kpc at  $z = 1.128$ , where the lobes are separated by 8 kpc. Inside X-ray galaxy groups, the smallest FR has  $D = 13.37$  kpc at  $z = 0.38$  with the most extended having  $D = 608.4$  kpc and  $z = 1.168$ ; this is also the most extended object in the Vardoulaki et al. (2021) FR sample. Future surveys with increased sensitivity and resolution will be able to resolve jets and lobes in AGN which appear compact at 3 GHz VLA-COSMOS. With future observations at larger sky areas and improved statistics, we will be in a better position to answer this question.

Nobels et al. (2022) show via hydrodynamical simulations of galaxy groups/clusters with masses above  $M_{200c} > 10^{13.5} M_{\odot}$ , like the ones studied here, a cyclical behaviour of AGN quenching and star formation activity: long periods where star formation is quenched by the AGN are followed by shorter periods of star formation and black hole accretion. This is because the reduction of AGN feedback makes the ICM unstable to precipitation and thus initiating a new episode of intense star formation. Furthermore, Pasini et al. (2020) report that feedback mechanisms in groups and clusters of galaxies are similar. In our study, we find that the AGN contribution to the galaxy groups RLF dominates at redshifts up to  $z_{\text{med}} = 0.8$ . The hosts of these AGN at 3 GHz VLA-COSMOS are quenched, based on the study of Vardoulaki et al. (2021). AGN at  $z_{\text{med}} = 0.8$  show low star-formation rates ( $\text{SFR}_{\text{med}} \sim 8 M_{\odot}/\text{yr}$ ) compared to SFGs at similar redshifts ( $\text{SFR}_{\text{med}} \sim 24 M_{\odot}/\text{yr}$ ). At lower redshifts ( $z_{\text{med}} = 0.3$ ), both AGN and SFGs populations show low median SFRs ( $\sim 1.2$  and  $\sim 3.4 M_{\odot}/\text{yr}$ , respectively). The median SFR in the field shows similar median values compared to the one inside galaxy groups for  $z_{\text{med}} = 0.3$  &  $0.8$ , for both AGN and SFGs.

To verify the cyclical behaviour presented in Nobels et al. (2022) a study of the duty cycle of individual objects is needed, which is beyond the scope of this analysis. A thorough analysis comparing AGN and SFGs in relation to large-scale environment is presented in Vardoulaki et al. (2021), and we refer the reader to that study. Detailed investigation of AGN feedback since  $z = 5$  at 3GHz COSMOS is presented in the studies of Smolčić et al. (2017c) and Ceraj et al. (2018).

Our analysis suggests that the bulk of high- $z$   $\log_{10}(M_{200c}/M_{\odot}) > 13.5$  groups must have been forming recently, and so the cooling has not been established. This is linked to the drop in occurrence of AGN in groups at high  $z$  by a factor of 6, suggesting that AGN feedback is lower by a factor of 6 at high redshifts. Hence, AGN feedback in the groups we are studying ( $\log_{10}(M_{200c}/M_{\odot})$  in the range 13.5-14.5) must be a recent phenomenon. There seems to be a change in the way groups operate above  $z > 1$ , with a faster evolution. Mass changes quickly and there is not enough time to virialise. Due to the lack of virialisation, the cooling does not start and the AGN activity is suppressed. This change can be triggered by 1) high thermalisation of matter, which is not sufficient in this case; 2) dynamically young groups where gas cooling does not happen.

On the other hand, low-mass groups form at  $z = 6$ . These are found to host radio AGN and have time to virialise, cool, and provide feedback. Additionally, cooling times for energetic electrons is much lower at high- $z$ .

## 6. Summary and Conclusions

We presented a study of radio luminosity functions, RLFs, of group galaxies in the COSMOS field, based on data from the VLA-COSMOS 3 GHz Large Project (Smolčić et al. 2017b) and the X-ray galaxy groups catalogue (Gozali et al. 2019, and in prep.). The X-ray galaxy groups cover halo masses in the range  $M_{200c} = 8 \times 10^{12} - 3 \times 10^{14} M_{\odot}$  and the redshift range  $0.07 < z < 2.3$ . To probe the same group population at all redshifts, we applied a halo-mass cut and only selected groups with halo masses  $M_{200c} > 10^{13.5} M_{\odot}$ . Furthermore, we applied completeness corrections to the calculation of the RLF (Novak et al. 2017) and all galaxy-group members are brighter than  $K = 24.5$  mag, which allows for an unbiased analysis.

We calculated the RLF of group galaxies based on the  $V_{\text{max}}$  method and compared it to the 3 GHz RLF from Novak et al. (2018) who fitted the total RLF with pure luminosity evolution models that depend on redshift. The AGN and SFG populations, characterised by the radio excess parameter, were fitted with a Markov chain Monte Carlo algorithm. We fitted the group galaxies' (GGs) RLFs using two methods, a) by scaling the total 3 GHz RLF, and b) with a linear (power-law) fit, and estimated their contribution to the total RLF. We also studied how much satellites (SGs), brightest group galaxies (BGGs), AGN, and SFGs contribute to the RLF of galaxy groups and to the total 3 GHz RLF. The two fitting methods provide similar results, with the ratio between data and model (Fig. 4) suggesting the power-law fit proving slightly better for the GG RLF. The linear regression fit is the adopted method for the interpretation of the results.

Our main results are summarised below:

1. The relative contribution of the group galaxies to the total 3 GHz radio luminosity function in galaxies in the COSMOS field generally decreases with increasing redshift, from 4% at low  $z$ , to 1% at  $z > 1$ , with an overdensity below  $z < 1$ , in line with large-scale structure studies of the COSMOS field.
2. The GG RLF has a low value at  $\sim 2$  down to  $z \sim 1.25$  followed by a sharp increase in the GG RLF at  $z \sim 1$  by a factor of 6, and then a smooth decline, which is driven mainly by satellite GGs. The latter suggests a mild evolution in the RLF of GGs from  $z \sim 1$  to 0.07 by a factor of 3.
3. The RLF of SGs dominates the RLF of group galaxies up to redshift of  $z \sim 1.2$ , where we observe a drop in the RLF of both BGGs and SGs.
4. The AGN dominate the GG RLF at  $z \sim 1$ , while the SFGs dominate the GG RLF at  $z_{\text{med}} = 1.2$ .

In summary, we observed a nearly flat but enhanced behavior of the contribution of galaxy groups to the total 3 GHz RLF up to  $z \sim 0.75$ , driven by SGs and AGN in GGs, followed by an increase and then a sharp drop, which agrees with the literature and is related to AGN occupying less massive halos above  $z > 1$ . The enhanced contribution and sharp drop are not driven by a possible sensitivity drop at high redshifts, but the actual abundance of massive groups, which is enhanced in high-density peaks with regards to normal galaxies, and which creates an enhancement of the fractional contribution of radio galaxies. In the case where all the galaxies would be groups of similar mass, but we would

**Table 3.** Fractional contribution  $f$  of the AGN and SFG linear (scaled; at  $\log_{10}(L_{1.4\text{ GHz}}/W\text{ Hz}^{-1}) = 23\&25$ ) RLF inside groups to the linear (scaled) GG RLF, and to the total RLF at  $L_{1.4\text{ GHz}} = 10^{25}$  and  $L_{1.4\text{ GHz}} = 10^{25} W\text{ Hz}^{-1}$ , as in Fig. 8.

$z_{\text{med}}$	$f_{\text{AGN-GG}}$	$f_{\text{AGN-tot23}}$	$f_{\text{AGN-tot25}}$	$f_{\text{SFG-GG}}$	$f_{\text{SFG-tot23}}$	$f_{\text{SFG-tot25}}$
0.3	3.55 (0.69; 0.99)	0.16 (0.06)	0.42 (0.25)	8.95 (0.30; $2 \times 10^{-5}$ )	0.41 (0.03)	1.06 ( $7 \times 10^{-6}$ )
0.6	0.56 (0.42; 0.99)	0.01 (0.02)	0.04 (0.13)	0.22 (0.57; $1 \times 10^{-4}$ )	0.01 (0.03)	0.01 ( $2 \times 10^{-5}$ )
0.8	0.33 (0.29; 0.99)	0.01 (0.03)	0.04 (0.33)	0.20 (0.70; $7 \times 10^{-4}$ )	0.01 (0.07)	0.03 ( $1 \times 10^{-4}$ )
1.2	0.31 (0.25; 0.99)	0.001 (0.003)	0.01 (0.03)	0.52 (0.74; $6 \times 10^{-5}$ )	0.002 (0.01)	0.01 ( $6 \times 10^{-5}$ )
1.9	–	–	–	0.16 (0.89; 0.02)	$4 \times 10^{-4}$ (0.01)	0.003 ( $6 \times 10^{-4}$ )

detect only some with X-rays, the ratio would have stayed the same, independent of the density of the field.

Another important result of this analysis is the RLF for group galaxies itself, as well as the contribution of the satellites and BGGs in group environments, which is a major observational constraint for tuning the models. Our study provides an observational probe for the accuracy of the numerical predictions of the radio emission in galaxies in a group environment. Finally, our results show a drop in occurrence of AGN in groups at high  $z$  by a factor of 6, suggesting that AGN feedback is lower by a factor of 6 at high redshifts. The bulk of high- $z$   $\log_{10}(M_{200c}/M_{\odot}) > 13.5$  groups must have been forming recently, and so the cooling has not been established. AGN at high- $z$  occupy low halo mass systems ( $\approx 10^{13.3} M_{\odot}$ ), revealing the details on the processes accountable for the galaxy evolution in massive environments.

*Acknowledgements.* We would like to thank Aritra Basu for useful discussions. We would like to thank the anonymous referee for a constructive report which significantly improved our manuscript. EV acknowledges support from Carl Zeiss Stiftung with the project code KODAR.

## References

- Barr, J. M., Bremer, M. N., Baker, J. C., & Lehnert, M. D. 2003, MNRAS, 346, 229
- Best, P., Lehnert, M., Röttgering, H., & Miley, G. 2002, in Astronomical Society of the Pacific Conference Series, Vol. 268, Tracing Cosmic Evolution with Galaxy Clusters, ed. S. Borgani, M. Mezzetti, & R. Valdamini, 19
- Best, P. N., Kauffmann, G., Heckman, T. M., & Ivezić, Ž. 2005, MNRAS, 362, 9
- Branchesi, M., Gioia, I. M., Fanti, C., Fanti, R., & Perley, R. 2006, A&A, 446, 97
- Byrd, G. & Valtonen, M. 1990, ApJ, 350, 89
- Ceraj, L., Smolčić, V., Delvecchio, I., et al. 2018, A&A, 620, A192
- Civano, F., Marchesi, S., Comastri, A., et al. 2016, ApJ, 819, 62
- Clemens, M. S., Vega, O., Bressan, A., et al. 2008, A&A, 477, 95
- Condon, J. J. 1984, ApJ, 287, 461
- Condon, J. J. 1992, ARA&A, 30, 575
- Condon, J. J., Cotton, W. D., & Broderick, J. J. 2002, AJ, 124, 675
- Delvecchio, I., Smolčić, V., Zamorani, G., et al. 2017, A&A, 602, A3
- Dressler, A. 1980, ApJ, 236, 351
- Elvis, M., Civano, F., Vignali, C., et al. 2009, ApJS, 184, 158
- Fanaroff, B. L. & Riley, J. M. 1974, MNRAS, 167, 31P
- Finoguenov, A., Guzzo, L., Hasinger, G., et al. 2007, ApJS, 172, 182
- Foreman-Mackey, D., Hogg, D. W., Lang, D., & Goodman, J. 2013, PASP, 125, 306
- George, M. R., Leauthaud, A., Bundy, K., et al. 2011, ApJ, 742, 125
- Gozaliasl, G., Finoguenov, A., Tanaka, M., et al. 2019, MNRAS, 483, 3545
- Grupponi, C., Pozzi, F., Rodighiero, G., et al. 2013, MNRAS, 432, 23
- Hale, C. L., Jarvis, M. J., Delvecchio, I., et al. 2018, MNRAS, 474, 4133
- Khosroshahi, H. G., Raouf, M., Miraghaei, H., et al. 2017, ApJ, 842, 81
- Laigle, C., McCracken, H. J., Ilbert, O., et al. 2016, ApJS, 224, 24
- Larson, R. B. 1980, Philosophical Transactions of the Royal Society of London Series A, 296, 299
- Leauthaud, A., Finoguenov, A., Kneib, J.-P., et al. 2010, ApJ, 709, 97
- Magorrian, J., Tremaine, S., Richstone, D., et al. 1998, AJ, 115, 2285
- Mauch, T. & Sadler, E. M. 2007, MNRAS, 375, 931
- Miller, N. A. & Owen, F. N. 2003, AJ, 125, 2427
- Nobels, F. S. J., Schaye, J., Schaller, M., Bahé, Y. M., & Chaikin, E. 2022, MNRAS, 515, 4838
- Novak, M., Smolčić, V., Delhaize, J., et al. 2017, A&A, 602, A5
- Novak, M., Smolčić, V., Schinnerer, E., et al. 2018, A&A, 614, A47
- Oemler, Augustus, J. 1974, ApJ, 194, 1
- Pasini, T., Brügger, M., de Gasperin, F., et al. 2020, MNRAS, 497, 2163
- Raouf, M., Khosroshahi, H. G., Mamon, G. A., et al. 2018, ApJ, 863, 40
- Reddy, N. A. & Yun, M. S. 2004, ApJ, 600, 695
- Sadler, E. M., Jackson, C. A., Cannon, R. D., et al. 2002, MNRAS, 329, 227
- Sadler, E. M., Jenkins, C. R., & Kotanyi, C. G. 1989, MNRAS, 240, 591
- Schinnerer, E., Sargent, M. T., Bondi, M., et al. 2010, ApJS, 188, 384
- Schmidt, M. 1968, ApJ, 151, 393
- Scoville, N., Arnouts, S., Aussel, H., et al. 2013, ApJS, 206, 3
- Scoville, N., Aussel, H., Brusa, M., et al. 2007, ApJS, 172, 1
- Smolčić, V., Delvecchio, I., Zamorani, G., et al. 2017a, A&A, 602, A2
- Smolčić, V., Novak, M., Bondi, M., et al. 2017b, A&A, 602, A1
- Smolčić, V., Novak, M., Delvecchio, I., et al. 2017c, A&A, 602, A6
- Tabatabaei, F. S., Schinnerer, E., Krause, M., et al. 2017, ApJ, 836, 185
- Vardoulaki, E., Jiménez Andrade, E. F., Delvecchio, I., et al. 2021, A&A, 648, A102
- Yuan, Z. S., Han, J. L., & Wen, Z. L. 2016, MNRAS, 460, 3669

**Appendix A: Numerical results from the calculation of the radio luminosity function in X-ray galaxy groups in COSMOS**

**Table A.1.** Radio properties of Group Galaxies in COSMOS

ID	3 GHz		radio		X-ray		Redshift z		$\log_{10}(L_X/10^{42} \text{ erg s}^{-1})$	$\log_{10}(M_{200c}/10^{13} M_\odot)$	$R_{200c}$ (deg.)	BGG Rank	Radio Class
	(1)	(2)	R.A. (3)	Dec. (deg., J2000.0) (4)	R.A. (5)	Dec. (6)	Radio (7)	X-ray (8)					
29	79	150.447297	2.053936	150.4456	2.054150	0.323	0.324 <sup>s</sup>	24.36	1.81 ± 0.86	1.73 ± 0.58	0.0417	0	AGN
35	333	150.042302	2.694820	150.04736	2.693170	0.218	0.219 <sup>s</sup>	23.50	1.03 ± 0.40	1.26 ± 0.43	0.0400	0	AGN
42	11	150.185632	1.661683	150.19728	1.658950	0.221	0.220 <sup>s</sup>	23.34	2.54 ± 0.75	2.23 ± 0.24	0.0838	5	AGN
44	237	150.110399	2.708261	150.11756	2.692520	0.351	0.349 <sup>s</sup>	24.48	2.19 ± 0.95	1.96 ± 0.52	0.0468	2	AGN
45	189	149.905915	2.396440	149.91816	2.388030	0.742	0.736 <sup>s</sup>	24.40	1.82 ± 1.30	1.58 ± 0.85	0.0209	3	AGN
61	134	149.649621	2.209249	149.6507	2.211630	0.954	0.951 <sup>s</sup>	23.85	2.27 ± 1.58	1.78 ± 0.88	0.0202	0	AGN
80	264	149.998389	2.769141	149.99834	2.774410	0.166	0.165 <sup>s</sup>	23.54	1.03 ± 0.45	1.28 ± 0.48	0.0516	0	AGN
88	52	150.44703	1.882829	150.44759	1.883190	0.670	0.672 <sup>s</sup>	24.02	1.84 ± 1.17	1.62 ± 0.74	0.0223	0	AGN
99	25	149.884002	1.750996	149.85402	1.770230	0.122	0.124 <sup>s</sup>	22.10	1.58 ± 0.08	1.65 ± 0.05	0.0884	0	AGN
103	143	150.207423	2.281893	150.22014	2.278510	0.917	0.885 <sup>s</sup>	24.53	2.18 ± 1.43	1.75 ± 0.79	0.0207	3	AGN
119	245	150.695821	2.760741	150.69144	2.754350	0.630	0.646 <sup>s</sup>	23.36	2.05 ± 1.34	1.76 ± 0.84	0.0257	2	AGN
127	187	149.623522	2.399203	149.62376	2.399380	0.846	0.840 <sup>s</sup>	24.10	2.33 ± 1.60	1.86 ± 0.92	0.0231	0	AGN
149	44	149.805372	1.874522	149.79852	1.872330	1.329	1.350 <sup>p</sup>	25.10	2.40 ± 1.98	1.71 ± 1.07	0.0155	0	AGN
156	217	150.007104	2.453454	150.0037	2.454870	0.731	0.732 <sup>s</sup>	24.14	1.73 ± 1.15	1.52 ± 0.73	0.0196	0	AGN
178	46	150.250884	1.863985	150.24614	1.865000	0.530	0.529 <sup>s</sup>	23.81	1.61 ± 1.01	1.52 ± 0.71	0.0246	0	AGN
182	190	149.441577	2.425937	149.45692	2.433530	0.481	0.484 <sup>s</sup>	24.03	2.16 ± 1.36	1.89 ± 0.89	0.0347	0	AGN
183	149	150.415664	2.430186	150.42235	2.428000	0.124	0.124 <sup>s</sup>	22.34	1.81 ± 0.16	1.79 ± 0.06	0.0986	0	AGN
187	311	149.942948	2.600608	149.93887	2.606860	0.344	0.342 <sup>s</sup>	24.84	1.50 ± 0.56	1.52 ± 0.38	0.0339	2	AGN
203	291	149.478815	2.521843	149.48956	2.516580	0.092	0.092 <sup>s</sup>	22.10	0.83 ± 0.12	1.17 ± 0.26	0.0806	84	SFG
211	215	150.172574	2.523342	150.17097	2.523630	0.697	0.697 <sup>s</sup>	24.14	1.58 ± 1.13	1.44 ± 0.77	0.0190	1	AGN
213	24	150.30117	1.689921	150.29169	1.689350	0.530	0.527 <sup>s</sup>	24.14	1.88 ± 1.02	1.70 ± 0.63	0.0281	1	AGN
220	203	149.666143	2.474287	149.65762	2.479720	0.956	0.948 <sup>s</sup>	23.50	2.28 ± 1.59	1.78 ± 0.89	0.0201	2	SFG
226	36	149.894896	1.764946	149.89491	1.764970	0.530	0.531 <sup>s</sup>	23.34	1.76 ± 1.09	1.61 ± 0.74	0.0262	1	AGN
235	20	150.325431	1.607013	150.32584	1.605100	0.222	0.227 <sup>s</sup>	23.01	1.13 ± 0.43	1.33 ± 0.42	0.0419	8	AGN
246	126	150.750943	2.199992	150.74525	2.196520	0.372	0.372 <sup>s</sup>	23.93	1.68 ± 0.99	1.62 ± 0.72	0.0345	0	SFG
251	173	150.058047	2.380425	150.05441	2.374090	0.347	0.347 <sup>s</sup>	22.63	1.37 ± 0.66	1.44 ± 0.51	0.0314	1	AGN
261	271	149.91793	2.701673	149.91853	2.700660	0.891	0.890 <sup>s</sup>	24.22	2.33 ± 1.60	1.84 ± 0.90	0.0221	4	AGN
278	302	150.090688	2.205629	150.09077	2.205680	0.426	0.427 <sup>s</sup>	23.37	1.01 ± 0.63	1.18 ± 0.57	0.0220	0	AGN
279	221	150.565828	2.496444	150.57024	2.498640	1.146	1.147 <sup>s</sup>	23.58	2.42 ± 2.01	1.80 ± 1.17	0.0183	0	AGN
302	14	150.247725	1.542408	150.24973	1.543310	0.886	0.886 <sup>p</sup>	24.21	2.50 ± 1.88	1.88 ± 1.06	0.0204	0	AGN

**Notes.** Basic radio properties of group galaxies in COSMOS. **Columns 1 & 2:** The 3 GHz radio ID (Smolčić et al. 2017b) and the X-ray galaxy group ID (Gozali et al. 2019, and in prep.), respectively. **Columns 3 & 4:** Right Ascension (R.A.) and Declination (Dec.) of the radio position in degrees, respectively. **Columns 5 & 6:** Right Ascension (R.A.) and Declination (Dec.) of the X-ray galaxy group position in degrees, respectively. **Columns 7 & 8:** Redshift of the radio source and the X-ray galaxy group, respectively. The character 's' denotes spectroscopic and 'p' denotes photometric redshift for the X-ray groups. **Column 9:** Radio luminosity at 1.4 GHz in  $\text{W Hz}^{-1}$ . **Column 10:** X-ray galaxy group luminosity and error in  $10^{42} \text{ erg s}^{-1}$ . **Column 11:** Halo mass at  $M_{200c}$  in  $10^{13} M_\odot$  and error. **Column 12:** Virial radius of the group  $R_{200c}$  in degrees. **Column 13:** BGG rank, where 0 denotes if the group galaxy is the brightest of the X-ray galaxy group and values  $> 0$  are for satellite galaxies. **Column 14:** Radio classification based on a combination of the radio excess parameter (Smolčić et al. 2017a; Delvechio et al. 2017) and objects having radio jets (Vardoulaki et al. 2021); 'AGN' exhibit radio excess or have radio jets, while 'SFG' do not.

Table A.1. Radio properties of Group Galaxies in COSMOS

3 GHz ID	X-ray		radio		X-ray		Redshift $z$		$\log_{10}(L_{1.4} \text{ GHz} / \text{W Hz}^{-1})$ (9)	$\log_{10}(L_X / 10^{42} \text{ erg s}^{-1})$ (10)	$\log_{10}(M_{200c} / 10^{13} M_{\odot})$ (11)	$R_{200c}$ (deg.) (12)	BGG Rank (13)	Radio Class (14)
	(2)	(3)	(4)	(5)	(6)	(7)	(8)							
309	10	150.721624	1.526961	150.75047	1.531030	0.680	0.669 <sup>s</sup>	24.62	2.64 ± 2.09	2.13 ± 1.36	0.0332	38	SFG	
315	17	149.964109	1.680330	149.96375	1.680220	0.372	0.373 <sup>s</sup>	23.19	2.24 ± 1.08	1.98 ± 0.62	0.0453	0	AGN	
316	88	150.502395	2.068242	150.49783	2.069730	0.438	0.438 <sup>s</sup>	23.14	1.69 ± 0.81	1.61 ± 0.52	0.0299	0	AGN	
337	124	150.056586	2.208546	150.05408	2.204690	0.188	0.186 <sup>s</sup>	22.50	0.86 ± 0.08	1.17 ± 0.17	0.0427	3	SFG	
351	124	150.057193	2.205909	150.05408	2.204690	0.186	0.186 <sup>s</sup>	22.63	0.86 ± 0.08	1.17 ± 0.17	0.0427	4	SFG	
364	208	149.561748	2.421941	149.55324	2.426060	0.848	0.843 <sup>s</sup>	24.38	2.27 ± 1.62	1.82 ± 0.96	0.0224	3	AGN	
368	99	149.792973	2.125628	149.78995	2.121450	0.353	0.353 <sup>s</sup>	23.22	1.05 ± 0.50	1.23 ± 0.47	0.0265	0	SFG	
370	174	149.648315	2.341367	149.64665	2.347520	0.978	0.964 <sup>s</sup>	23.87	2.54 ± 1.74	1.95 ± 0.95	0.0230	0	AGN	
376	27	150.426473	1.682758	150.42935	1.680110	0.218	0.217 <sup>s</sup>	22.38	0.81 ± 0.40	1.12 ± 0.49	0.0359	0	AGN	
389	220	149.915703	2.521334	149.92079	2.521660	0.729	0.729 <sup>s</sup>	23.73	3.05 ± 1.49	2.37 ± 0.61	0.0376	2	AGN	
409	394	149.81884	2.162316	149.81022	2.148230	0.354	0.354 <sup>s</sup>	23.16	1.52 ± 0.89	1.51 ± 0.67	0.0323	0	AGN	
437	107	149.596841	2.149863	149.6049	2.146700	0.283	0.282 <sup>s</sup>	24.10	1.09 ± 0.43	1.28 ± 0.41	0.0328	52	AGN	
442	246	149.761345	2.929088	149.76143	2.926720	0.349	0.350 <sup>s</sup>	23.37	2.59 ± 1.52	2.21 ± 0.95	0.0568	0	SFG	
443	87	150.510625	2.029236	150.5111	2.026990	0.899	0.899 <sup>p</sup>	24.25	1.94 ± 1.61	1.59 ± 1.03	0.0180	0	AGN	
449	150	149.983234	2.317168	149.98035	2.314270	0.934	0.933 <sup>s</sup>	24.09	2.35 ± 1.48	1.84 ± 0.76	0.0214	0	AGN	
452	22	150.703654	1.648621	150.70383	1.651080	0.694	0.694 <sup>p</sup>	24.11	1.98 ± 1.43	1.69 ± 0.94	0.0231	3	AGN	
502	124	150.075847	2.203358	150.05408	2.204690	0.185	0.186 <sup>s</sup>	22.21	0.86 ± 0.08	1.17 ± 0.17	0.0427	59	AGN	
508	11	150.202249	1.653862	150.19728	1.658950	0.218	0.220 <sup>s</sup>	22.23	2.54 ± 0.75	2.23 ± 0.24	0.0838	1	AGN	
513	163	150.027738	2.373876	150.02875	2.374780	0.222	0.221 <sup>s</sup>	22.17	0.97 ± 0.17	1.22 ± 0.22	0.0385	0	SFG	
524	288	149.885162	2.581119	149.87827	2.574060	0.694	0.694 <sup>s</sup>	23.20	1.97 ± 1.20	1.69 ± 0.71	0.0230	2	AGN	
528	237	150.123446	2.671712	150.11756	2.692520	0.345	0.349 <sup>s</sup>	23.12	2.19 ± 0.95	1.96 ± 0.52	0.0468	6	AGN	
541	115	149.846232	2.141005	149.85056	2.139020	0.371	0.371 <sup>s</sup>	22.57	1.97 ± 1.49	1.63 ± 0.93	0.0194	0	SFG	
566	239	150.105072	2.724567	150.10533	2.723920	0.729	0.731 <sup>s</sup>	24.18	1.87 ± 1.33	1.61 ± 0.85	0.0211	0	AGN	
584	259	149.649623	2.831876	149.65741	2.822050	0.705	0.702 <sup>s</sup>	23.65	2.00 ± 1.27	1.71 ± 0.77	0.0232	0	AGN	
601	369	150.472278	2.324637	150.46835	2.326680	0.894	0.886 <sup>s</sup>	24.00	1.93 ± 1.28	1.55 ± 0.69	0.0174	0	AGN	
616	362	149.62836	2.076451	149.62906	2.066010	0.304	0.313 <sup>s</sup>	22.78	1.03 ± 0.49	1.21 ± 0.46	0.0284	2	AGN	
620	13	149.582333	1.605560	149.5823	1.605570	0.840	0.848 <sup>p</sup>	23.19	2.31 ± 1.71	1.85 ± 1.04	0.0228	0	AGN	
627	282	150.355695	2.647710	150.35358	2.643340	0.396	0.396 <sup>s</sup>	22.77	1.35 ± 0.65	1.41 ± 0.49	0.0277	0	AGN	
637	167	150.096113	2.298559	150.09583	2.299060	0.360	0.361 <sup>s</sup>	22.32	1.24 ± 0.56	1.35 ± 0.46	0.0286	1	SFG	
639	378	150.444606	2.547666	150.45257	2.551110	0.348	0.348 <sup>s</sup>	22.59	1.09 ± 0.48	1.24 ± 0.41	0.0266	0	AGN	
648	215	150.166524	2.521684	150.17097	2.523630	0.698	0.697 <sup>s</sup>	23.27	1.58 ± 1.13	1.44 ± 0.77	0.0190	3	AGN	
671	155	150.594594	2.537682	150.59137	2.537780	1.153	1.138 <sup>p</sup>	24.03	2.50 ± 1.81	1.89 ± 0.99	0.0208	1	AGN	
682	93	149.665396	2.091182	149.66565	2.075670	0.340	0.339 <sup>s</sup>	22.24	1.54 ± 0.85	1.55 ± 0.65	0.0349	55	AGN	
691	124	150.06689	2.210364	150.05408	2.204690	0.187	0.186 <sup>s</sup>	22.70	0.86 ± 0.08	1.17 ± 0.17	0.0427	0	SFG	
712	192	150.159368	2.391054	150.1537	2.397640	0.872	0.897 <sup>s</sup>	23.42	2.00 ± 1.35	1.63 ± 0.77	0.0186	1	SFG	
733	148	150.576667	2.255487	150.58372	2.259020	0.672	0.672 <sup>p</sup>	23.11	1.71 ± 1.23	1.53 ± 0.83	0.0209	0	SFG	
738	267	150.446883	2.749550	150.44487	2.753930	1.165	1.138 <sup>s</sup>	23.95	2.58 ± 1.90	1.91 ± 1.01	0.0199	0	AGN	
739	145	149.811117	2.252509	149.82838	2.261260	0.380	0.379 <sup>s</sup>	22.86	1.31 ± 0.59	1.38 ± 0.46	0.0282	0	AGN	
759	172	149.929268	2.409000	149.93372	2.409940	0.903	0.874 <sup>p</sup>	23.53	1.94 ± 1.31	1.60 ± 0.76	0.0185	0	AGN	
773	37	149.564552	1.823094	149.57253	1.816800	1.507	1.508 <sup>p</sup>	24.84	2.90 ± 2.50	1.97 ± 1.36	0.0178	20	AGN	

Notes. (Continued)

Table A.1. Radio properties of Group Galaxies in COSMOS

3 GHz (1)	radio		X-ray		Redshift z		$\log_{10}(L_{1.4 \text{ GHz}} / \text{W Hz}^{-1})$ (9)	$\log_{10}(L_X / 10^{42} \text{ erg s}^{-1})$ (10)	$\log_{10}(M_{200c} / 10^{13} M_{\odot})$ (11)	$R_{200c}$ (deg.) (12)	BGG Rank (13)	Radio Class (14)	
	ID 3 GHz	X-ray	R.A. (3)	Dec. (deg., J2000.0) (4)	R.A. (5)	Dec. (6)							Radio (7)
832	63	150.360853	1.931518	150.353324	1.933030	1.234	1.233 <sup>P</sup>	23.77	2.38 ± 1.79	1.74 ± 0.94	0.0167	1	AGN
846	282	150.359573	2.659472	150.353358	2.643340	0.397	0.396 <sup>S</sup>	22.27	1.35 ± 0.65	1.41 ± 0.49	0.0277	1	AGN
879	322	150.228073	2.269746	150.2254	2.268730	0.678	0.677 <sup>P</sup>	23.37	1.65 ± 1.16	1.49 ± 0.78	0.0202	1	SFG
888	193	150.090874	2.391224	150.0918	2.393330	0.221	0.220 <sup>S</sup>	22.30	1.41 ± 0.29	1.51 ± 0.18	0.0481	0	AGN
909	358	149.479617	1.972097	149.49591	1.972860	0.290	0.272 <sup>S</sup>	22.77	1.44 ± 0.61	1.49 ± 0.46	0.0395	7	AGN
952	343	150.408683	2.777262	150.39865	2.762250	0.832	0.818 <sup>S</sup>	23.36	2.53 ± 1.73	2.00 ± 0.99	0.0263	7	SFG
954	30	150.242515	1.766379	150.24672	1.772280	0.623	0.626 <sup>S</sup>	23.26	1.67 ± 1.14	1.56 ± 0.82	0.0253	0	AGN
958	203	149.659963	2.465061	149.65762	2.479720	0.958	0.948 <sup>S</sup>	23.94	2.28 ± 1.59	1.78 ± 0.89	0.0201	0	AGN
963	68	149.988307	1.965538	149.9996	1.973280	0.598	0.600 <sup>S</sup>	22.89	1.64 ± 1.06	1.51 ± 0.72	0.0223	1	AGN
987	373	149.551723	2.437181	149.54971	2.432490	0.843	0.843 <sup>S</sup>	23.62	2.07 ± 1.45	1.66 ± 0.83	0.0195	0	AGN
988	384	149.625426	2.921988	149.6306	2.901520	0.472	0.489 <sup>S</sup>	23.18	1.63 ± 1.16	1.52 ± 0.83	0.0251	2	SFG
991	120	150.506703	2.253738	150.50516	2.225070	0.837	0.835 <sup>S</sup>	23.59	2.95 ± 1.61	2.26 ± 0.72	0.0317	1	SFG
995	173	150.080596	2.390270	150.05441	2.374090	0.353	0.347 <sup>S</sup>	22.60	1.37 ± 0.66	1.44 ± 0.51	0.0314	0	AGN
997	395	149.815162	2.149065	149.8261	2.135200	0.168	0.169 <sup>S</sup>	22.06	0.09 ± -0.10	0.67 ± 0.24	0.0314	1	SFG
1008	356	150.652153	1.877237	150.6687	1.875570	0.410	0.386 <sup>S</sup>	22.96	1.23 ± 0.62	1.31 ± 0.48	0.0249	1	SFG
1015	223	150.058689	2.477400	150.05064	2.475200	1.258	1.260 <sup>P</sup>	24.06	2.43 ± 1.87	1.76 ± 0.99	0.0168	16	SFG
1030	174	149.657792	2.354473	149.64665	2.347520	0.990	0.964 <sup>S</sup>	23.32	2.54 ± 1.74	1.95 ± 0.95	0.0230	10	AGN
1034	125	150.616524	2.167938	150.62251	2.160390	1.505	1.500 <sup>P</sup>	24.94	2.62 ± 2.26	1.81 ± 1.23	0.0161	1	SFG
1042	222	150.575608	2.500534	150.57957	2.478980	0.611	0.610 <sup>S</sup>	23.20	1.63 ± 1.20	1.51 ± 0.86	0.0219	0	SFG
1079	378	150.477031	2.548821	150.45257	2.551110	0.374	0.348 <sup>S</sup>	22.63	1.09 ± 0.48	1.24 ± 0.41	0.0266	5	SFG
1114	159	150.344818	2.283020	150.34819	2.282180	0.373	0.372 <sup>S</sup>	22.80	1.21 ± 0.58	1.33 ± 0.48	0.0274	0	SFG
1132	355	150.371233	1.849033	150.36924	1.853530	0.461	0.461 <sup>S</sup>	22.90	1.19 ± 0.67	1.26 ± 0.52	0.0218	0	SFG
1147	11	150.198432	1.671827	150.19728	1.658950	0.216	0.220 <sup>S</sup>	22.71	2.54 ± 0.75	2.23 ± 0.24	0.0838	10	SFG
1156	119	150.34591	2.147508	150.34628	2.143840	1.256	1.230 <sup>P</sup>	24.16	2.30 ± 1.89	1.69 ± 1.06	0.0161	1	SFG
1173	215	150.173484	2.523633	150.17097	2.523630	0.696	0.697 <sup>S</sup>	23.30	1.58 ± 1.13	1.44 ± 0.77	0.0190	2	AGN
1179	11	150.18977	1.657352	150.19728	1.658950	0.223	0.220 <sup>S</sup>	22.45	2.54 ± 0.75	2.23 ± 0.24	0.0838	0	AGN
1249	120	150.507659	2.210760	150.50516	2.225070	0.829	0.835 <sup>S</sup>	23.71	2.95 ± 1.61	2.26 ± 0.72	0.0317	32	AGN
1262	298	149.79962	2.140057	149.7899	2.121400	0.354	0.354 <sup>P</sup>	23.08	1.12 ± 0.83	1.27 ± 0.76	0.0273	3	SFG
1276	194	149.700891	2.402565	149.70296	2.400810	0.376	0.364 <sup>S</sup>	22.77	1.34 ± 0.80	1.41 ± 0.66	0.0304	7	SFG
1298	352	149.691746	1.818160	149.69172	1.814420	0.738	0.755 <sup>S</sup>	23.29	1.67 ± 1.31	1.44 ± 0.87	0.0181	0	AGN
1342	237	150.143348	2.686859	150.11756	2.692520	0.345	0.349 <sup>S</sup>	22.59	2.19 ± 0.95	1.96 ± 0.52	0.0468	0	AGN
1348	118	149.626146	2.140052	149.63382	2.136720	0.946	0.944 <sup>S</sup>	23.80	2.12 ± 1.55	1.68 ± 0.89	0.0186	4	SFG
1358	312	150.545968	2.714987	150.54362	2.717990	0.262	0.262 <sup>P</sup>	22.19	0.92 ± 0.45	1.18 ± 0.49	0.0323	0	SFG
1397	155	150.592978	2.538922	150.59137	2.537780	1.138	1.138 <sup>P</sup>	23.70	2.50 ± 1.81	1.89 ± 0.99	0.0208	0	AGN
1405	262	149.590751	2.805776	149.59956	2.819910	0.339	0.342 <sup>S</sup>	22.92	2.24 ± 1.00	2.00 ± 0.55	0.0488	15	SFG
1415	245	150.706808	2.762515	150.69144	2.754350	0.662	0.646 <sup>S</sup>	23.23	2.05 ± 1.34	1.76 ± 0.84	0.0257	0	AGN
1441	92	150.211767	2.068341	150.21114	2.069810	0.370	0.371 <sup>S</sup>	22.58	0.76 ± 0.50	1.04 ± 0.54	0.0221	0	AGN
1448	396	150.573507	1.933847	150.5619	1.918000	0.310	0.310 <sup>S</sup>	22.72	1.15 ± 0.45	1.29 ± 0.38	0.0305	1	AGN
1464	138	149.510262	2.260158	149.50941	2.261110	0.947	0.937 <sup>S</sup>	23.76	2.53 ± 1.86	1.95 ± 1.07	0.0231	2	AGN
1469	218	149.774641	2.471147	149.77321	2.463440	0.735	0.735 <sup>P</sup>	23.32	1.53 ± 1.20	1.39 ± 0.84	0.0177	1	SFG

Notes. (Continued)

Table A.1. Radio properties of Group Galaxies in COSMOS

ID	3 GHz		radio		X-ray		Redshift z		$\log_{10}(L_{1.4 \text{ GHz}} / \text{W Hz}^{-1})$	$\log_{10}(L_X / 10^{42} \text{ erg s}^{-1})$	$\log_{10}(M_{200c} / 10^{13} M_{\odot})$	$R_{200c}$ (deg.)	BGG Rank	Radio Class
	(1)	(2)	R.A. (3)	Dec. (4)	R.A. (5)	Dec. (6)	Radio (7)	X-ray (8)						
1495	254	150.10643	2.794748	150.09665	2.806100	0.729	0.701 <sup>s</sup>	23.39	1.99 ± 1.46	1.70 ± 0.96	0.0232	1	AGN	
1503	88	150.484941	2.082487	150.49783	2.069730	0.428	0.438 <sup>s</sup>	22.78	1.69 ± 0.81	1.61 ± 0.52	0.0299	12	SFG	
1535	241	150.490648	2.747902	150.4879	2.751180	0.612	0.611 <sup>s</sup>	23.03	1.82 ± 1.21	1.62 ± 0.80	0.0240	0	AGN	
1538	29	150.168574	1.785039	150.18167	1.770860	0.345	0.344 <sup>s</sup>	22.50	1.95 ± 0.72	1.81 ± 0.38	0.0422	3	AGN	
1549	237	150.108009	2.695533	150.11756	2.692520	0.349	0.349 <sup>s</sup>	22.52	2.19 ± 0.95	1.96 ± 0.52	0.0468	16	SFG	
1633	21	150.173228	1.597977	150.14821	1.603690	0.360	0.345 <sup>p</sup>	22.55	1.72 ± 1.15	1.59 ± 0.81	0.0262	1	SFG	
1647	267	150.435892	2.758884	150.44487	2.753930	1.140	1.138 <sup>s</sup>	23.80	2.58 ± 1.90	1.91 ± 1.01	0.0199	5	AGN	
1653	123	150.018889	2.147805	150.02039	2.145630	0.959	0.957 <sup>s</sup>	23.65	1.88 ± 1.43	1.53 ± 0.86	0.0166	0	SFG	
1675	256	149.466118	2.900144	149.4375	2.901190	0.330	0.310 <sup>p</sup>	22.87	1.45 ± 1.02	1.50 ± 0.85	0.0361	2	AGN	
1695	153	150.327763	2.277063	150.32233	2.282580	0.980	0.973 <sup>s</sup>	23.38	2.11 ± 1.49	1.67 ± 0.83	0.0182	1	SFG	
1736	221	150.567262	2.503606	150.57024	2.498640	1.146	1.147 <sup>s</sup>	23.42	2.42 ± 2.01	1.80 ± 1.17	0.0183	11	SFG	
1754	222	150.570208	2.498649	150.57957	2.478980	0.608	0.610 <sup>s</sup>	23.02	1.63 ± 1.20	1.51 ± 0.86	0.0219	1	AGN	
1755	77	150.3128	2.009030	150.3172	2.004710	0.311	0.311 <sup>s</sup>	22.35	1.15 ± 0.47	1.31 ± 0.42	0.0311	0	SFG	
1795	304	150.413139	2.409916	150.41328	2.409970	0.385	0.385 <sup>s</sup>	22.52	1.89 ± 0.74	1.75 ± 0.41	0.0371	0	AGN	
1798	386	150.653868	2.841151	150.65611	2.840200	0.250	0.248 <sup>s</sup>	22.28	1.09 ± 0.46	1.28 ± 0.43	0.0359	0	AGN	
1829	144	149.839129	2.226169	149.84988	2.231150	0.943	0.931 <sup>s</sup>	23.64	1.65 ± 1.21	1.45 ± 0.79	0.0176	0	AGN	
1852	42	149.521503	1.885132	149.52252	1.882410	0.530	0.530 <sup>s</sup>	22.98	1.74 ± 1.21	1.61 ± 0.86	0.0262	1	AGN	
1902	292	150.030348	2.559337	150.03386	2.551700	0.603	0.746 <sup>s</sup>	22.95	1.65 ± 1.34	1.46 ± 0.93	0.0185	3	SFG	
1912	115	149.843394	2.147605	149.85056	2.139020	0.352	0.371 <sup>s</sup>	22.43	1.97 ± 1.49	1.63 ± 0.93	0.0194	1	SFG	
1954	32	150.220237	1.743173	150.23296	1.739570	0.950	0.980 <sup>p</sup>	23.60	2.05 ± 1.54	1.63 ± 0.90	0.0177	5	AGN	
1962	332	150.035037	2.553154	150.03384	2.551770	0.884	0.899 <sup>s</sup>	23.33	1.84 ± 1.39	1.53 ± 0.86	0.0174	0	AGN	
1967	25	149.890626	1.818286	149.85402	1.770230	0.133	0.124 <sup>s</sup>	22.53	1.58 ± 0.08	1.65 ± -0.05	0.0884	13	SFG	
1983	271	149.905567	2.718306	149.91853	2.700660	0.880	0.890 <sup>s</sup>	23.32	2.33 ± 1.60	1.84 ± 0.90	0.0221	0	AGN	
2016	63	150.349433	1.937071	150.35324	1.933030	1.232	1.233 <sup>p</sup>	23.41	2.38 ± 1.79	1.74 ± 0.94	0.0167	3	SFG	
2022	39	149.812709	1.823971	149.82126	1.825430	0.530	0.531 <sup>s</sup>	22.78	1.74 ± 1.00	1.60 ± 0.66	0.0260	2	SFG	
2039	167	150.095083	2.300492	150.09583	2.299060	0.361	0.361 <sup>s</sup>	22.52	1.24 ± 0.56	1.35 ± 0.46	0.0286	0	AGN	
2048	215	150.166624	2.525302	150.17097	2.523630	0.694	0.697 <sup>s</sup>	22.93	1.58 ± 1.13	1.44 ± 0.77	0.0190	0	SFG	
2053	71	150.359932	2.004580	150.36566	2.002520	0.832	0.828 <sup>s</sup>	23.23	2.12 ± 1.39	1.73 ± 0.80	0.0212	4	AGN	
2109	4	149.676058	1.550761	149.67828	1.530020	0.651	0.653 <sup>p</sup>	23.38	2.31 ± 1.42	1.98 ± 0.89	0.0370	1	SFG	
2118	398	150.539396	1.923583	150.544	1.922700	0.464	0.463 <sup>s</sup>	23.03	1.59 ± 0.80	1.51 ± 0.51	0.0263	3	SFG	
2194	24	150.310117	1.673725	150.29169	1.689350	0.527	0.527 <sup>s</sup>	23.09	1.88 ± 1.02	1.70 ± 0.63	0.0281	5	SFG	
2218	25	149.851714	1.781046	149.85402	1.770230	0.127	0.124 <sup>s</sup>	21.52	1.58 ± 0.08	1.65 ± -0.05	0.0884	2	SFG	
2225	343	150.397679	2.761617	150.39865	2.762250	0.817	0.818 <sup>s</sup>	23.20	2.53 ± 1.73	2.00 ± 0.99	0.0263	2	AGN	
2241	373	149.544976	2.441755	149.54971	2.432490	0.848	0.843 <sup>s</sup>	23.30	2.07 ± 1.45	1.66 ± 0.83	0.0195	1	SFG	
2258	310	150.54854	2.498689	150.55296	2.499640	0.881	0.879 <sup>s</sup>	23.29	2.14 ± 1.69	1.73 ± 1.06	0.0203	0	SFG	
2273	269	150.237282	2.689222	150.2357	2.681610	1.264	1.310 <sup>p</sup>	23.98	2.86 ± 2.17	1.83 ± 0.94	0.0143	0	SFG	
2318	236	150.234964	2.736515	150.21767	2.737930	0.960	0.923 <sup>s</sup>	23.43	2.12 ± 1.51	1.69 ± 0.87	0.0190	2	SFG	
2329	220	149.904547	2.552293	149.92079	2.521660	0.759	0.729 <sup>s</sup>	23.06	3.05 ± 1.49	2.37 ± 0.61	0.0376	134	AGN	
2381	234	150.161887	2.601258	150.16257	2.612660	0.888	0.892 <sup>s</sup>	23.30	2.03 ± 1.40	1.65 ± 0.81	0.0190	1	AGN	
2425	142	150.28462	2.278840	150.28607	2.278140	0.122	0.123 <sup>s</sup>	21.34	0.62 ± -0.21	1.03 ± -0.00	0.0559	0	SFG	

Notes. (Continued)

**Table A.1.** Radio properties of Group Galaxies in COSMOS

3 GHz		X-ray		radio		Dec.		R.A.		X-ray		Radio		Redshift z		$L_{1.4}$ GHz/ W Hz <sup>-1</sup> )		$\log_{10}(L_X/10^{42} \text{ erg s}^{-1})$		$\log_{10}(M_{200c}/10^{13} M_{\odot})$		BGG		Radio			
(1)	(2)	(3)	(4)	(5)	(6)	(7)	(8)	(9)	(10)	(11)	(12)	(13)	(14)	(15)	(16)	(17)	(18)	(19)	(20)	(21)	(22)	(23)	(24)	(25)	(26)	(27)	(28)
2456	4	149.678007	1.550514	149.67828	1.530020	0.630	0.653 <sup>p</sup>	23.13	2.31 ± 1.42	1.98 ± 0.89	0.0370	0	AGN														
2486	25	149.885327	1.753499	149.85402	1.770230	0.141	0.124 <sup>s</sup>	21.49	1.58 ± 0.08	1.65 ± -0.05	0.0884	20	SFG														
2500	304	150.384362	2.391270	150.41328	2.409970	0.374	0.385 <sup>s</sup>	22.61	1.89 ± 0.74	1.75 ± 0.41	0.0371	6	SFG														
2509	381	150.151975	2.860138	150.17971	2.852160	0.323	0.306 <sup>s</sup>	22.64	1.17 ± 0.60	1.31 ± 0.52	0.0307	2	SFG														
2526	149	150.431056	2.402741	150.42235	2.428000	0.124	0.124 <sup>s</sup>	21.46	1.81 ± 0.16	1.79 ± -0.06	0.0986	4	SFG														
2539	225	150.230528	2.495026	150.2292	2.476260	0.374	0.374 <sup>s</sup>	23.14	1.43 ± 0.58	1.46 ± 0.41	0.0304	1	AGN														
2548	110	150.179814	2.110308	150.17787	2.113960	0.360	0.361 <sup>s</sup>	22.72	1.31 ± 0.92	1.40 ± 0.78	0.0297	4	SFG														
2589	203	149.675092	2.475447	149.65762	2.479720	0.966	0.948 <sup>s</sup>	23.43	2.28 ± 1.59	1.78 ± 0.89	0.0201	5	SFG														
2590	377	150.132329	2.523302	150.134	2.525820	1.319	1.319 <sup>s</sup>	23.63	2.26 ± 1.75	1.59 ± 0.86	0.0141	4	SFG														
2632	218	149.788781	2.466447	149.77321	2.463440	0.719	0.735 <sup>p</sup>	23.05	1.53 ± 1.20	1.39 ± 0.84	0.0177	0	AGN														
2641	106	150.090151	2.173880	150.10504	2.164490	0.682	0.682 <sup>s</sup>	22.96	2.03 ± 1.19	1.73 ± 0.68	0.0242	0	AGN														
2653	343	150.397629	2.768056	150.39865	2.762250	0.838	0.818 <sup>s</sup>	23.16	2.53 ± 1.73	2.00 ± 0.99	0.0263	18	AGN														
2719	188	150.537767	2.413637	150.53645	2.406740	0.618	0.617 <sup>p</sup>	23.07	1.73 ± 1.09	1.56 ± 0.71	0.0227	0	SFG														
2818	40	150.42615	1.854896	150.4125	1.848880	0.968	0.973 <sup>s</sup>	23.32	2.49 ± 1.56	1.92 ± 0.78	0.0221	0	AGN														
2831	311	149.937997	2.606273	149.93887	2.606860	0.344	0.342 <sup>s</sup>	22.28	1.50 ± 0.56	1.52 ± 0.38	0.0339	0	AGN														
2907	145	149.824304	2.265368	149.82838	2.261260	0.378	0.379 <sup>s</sup>	22.36	1.31 ± 0.59	1.38 ± 0.46	0.0282	2	SFG														
2939	6	150.287274	1.566764	150.29951	1.553430	0.346	0.360 <sup>s</sup>	22.77	2.06 ± 1.01	1.87 ± 0.62	0.0425	10	SFG														
2973	11	150.228634	1.657480	150.19728	1.658950	0.219	0.220 <sup>s</sup>	22.04	2.54 ± 0.75	2.23 ± 0.24	0.0838	54	SFG														
2976	295	150.419896	1.975530	150.42104	1.984480	0.310	0.323 <sup>s</sup>	22.15	1.20 ± 0.67	1.34 ± 0.59	0.0309	2	SFG														
2996	207	149.791776	2.445545	149.78217	2.449350	0.260	0.262 <sup>s</sup>	22.93	1.72 ± 1.13	1.53 ± 0.73	0.0209	0	AGN														
3010	227	150.22866	2.553902	150.2393	2.560340	0.226	0.220 <sup>s</sup>	22.05	1.17 ± 0.24	1.35 ± 0.22	0.0426	1	SFG														
3021	29	150.181213	1.740722	150.18167	1.770860	0.358	0.344 <sup>s</sup>	22.49	1.95 ± 0.72	1.81 ± 0.38	0.0422	13	SFG														
3034	201	150.107983	2.449213	150.10431	2.420810	0.217	0.223 <sup>s</sup>	21.78	1.13 ± 0.18	1.32 ± 0.18	0.0416	13	SFG														
3053	406	150.457359	1.964530	150.45897	1.972880	2.241	2.250 <sup>p</sup>	24.09	3.00 ± 2.39	1.74 ± 0.91	0.0119	0	SFG														
3087	246	149.759651	2.918628	149.76143	2.926720	0.355	0.350 <sup>s</sup>	22.62	2.59 ± 1.52	2.21 ± 0.95	0.0568	20	SFG														
3130	135	150.103543	2.197895	150.09421	2.198250	0.682	0.682 <sup>s</sup>	22.89	1.61 ± 1.08	1.46 ± 0.72	0.0196	2	AGN														
3135	275	149.83895	2.675072	149.83842	2.675170	0.260	0.264 <sup>s</sup>	23.12	1.28 ± 0.82	1.41 ± 0.73	0.0388	0	SFG														
3192	11	150.147624	1.632187	150.19728	1.658950	0.230	0.220 <sup>s</sup>	22.10	2.54 ± 0.75	2.23 ± 0.24	0.0838	34	SFG														
3238	64	150.188839	1.984626	150.19821	1.985060	0.440	0.440 <sup>s</sup>	22.48	1.53 ± 0.74	1.51 ± 0.51	0.0278	3	SFG														
3349	199	150.687598	2.285660	150.70682	2.292530	1.114	1.095 <sup>s</sup>	23.41	2.01 ± 1.66	1.70 ± 1.13	0.0226	2	SFG														
3367	289	150.104331	2.546902	150.11438	2.555190	0.497	0.502 <sup>s</sup>	22.70	1.62 ± 0.96	1.54 ± 0.66	0.0258	1	AGN														
3382	143	150.210349	2.291389	150.22014	2.278510	0.877	0.885 <sup>s</sup>	23.15	2.18 ± 1.43	1.75 ± 0.79	0.0207	7	SFG														
3407	383	149.601276	2.850213	149.59999	2.850310	0.837	0.843 <sup>s</sup>	23.15	2.01 ± 1.47	1.61 ± 0.86	0.0189	1	SFG														
3410	212	149.870027	2.443161	149.88141	2.448430	0.333	0.358 <sup>s</sup>	22.63	1.56 ± 0.63	1.55 ± 0.42	0.0336	7	SFG														
3414	9	150.51942	1.560995	150.50597	1.542640	0.928	1.100 <sup>p</sup>	23.36	2.82 ± 2.23	2.08 ± 1.27	0.0232	0	AGN														
3474	351	150.179668	1.816644	150.16592	1.807820	0.338	0.343 <sup>s</sup>	22.21	1.16 ± 0.57	1.28 ± 0.48	0.0281	0	SFG														
3492	216	150.06149	2.647200	150.06644	2.644100	0.697	0.696 <sup>s</sup>	22.90	1.86 ± 1.25	1.62 ± 0.80	0.0219	0	SFG														
3493	120	150.508104	2.219988	150.50516	2.225070	0.833	0.835 <sup>s</sup>	23.62	2.95 ± 1.61	2.26 ± 0.72	0.0317	44	SFG														
3523	368	150.377351	2.311777	150.37198	2.309470	2.147	2.149 <sup>s</sup>	24.14	2.89 ± 2.37	1.71 ± 0.98	0.0120	0	SFG														
3550	408	150.582031	2.091601	150.59004	2.091380	1.212	1.200 <sup>p</sup>	23.46	2.40 ± 1.79	1.72 ± 0.90	0.0164	0	SFG														

**Notes.** (Continued)

Table A.1. Radio properties of Group Galaxies in COSMOS

3 GHz ID	X-ray	radio		X-ray		Redshift $z$		$\log_{10}(L_{1.4 \text{ GHz}} / \text{W Hz}^{-1})$ (9)	$\log_{10}(L_X / 10^{42} \text{ erg s}^{-1})$ (10)	$\log_{10}(M_{200c} / 10^{13} M_{\odot})$ (11)	$R_{200c}$ (deg.) (12)	BGG Rank (13)	Radio Class (14)
		R.A. (3)	Dec. (deg., J2000.0) (4)	R.A. (5)	Dec. (6)	Radio (7)	X-ray (8)						
3556	186	150.211565	2.401837	150.21205	2.402810	0.904	0.904 <sup>s</sup>	23.15	2.20 ± 1.44	1.75 ± 0.78	0.0204	2	SFG
3581	217	149.997322	2.449265	150.0037	2.454870	0.759	0.732 <sup>s</sup>	23.36	1.73 ± 1.15	1.52 ± 0.73	0.0196	7	AGN
3643	128	150.575167	2.162272	150.58504	2.182050	0.533	0.543 <sup>s</sup>	22.61	1.67 ± 1.02	1.55 ± 0.69	0.0242	2	AGN
3653	152	149.621697	2.261863	149.61397	2.268890	0.946	0.975 <sup>s</sup>	23.66	2.32 ± 1.86	1.80 ± 1.12	0.0201	8	SFG
3654	183	150.481311	2.375342	150.48979	2.384890	1.201	1.170 <sup>p</sup>	23.40	2.16 ± 1.64	1.62 ± 0.88	0.0155	1	SFG
3670	6	150.298468	1.554236	150.29951	1.553430	0.360	0.360 <sup>s</sup>	22.93	2.06 ± 1.01	1.87 ± 0.62	0.0425	2	AGN
3708	400	150.712179	1.588094	150.71222	1.586070	1.757	1.800 <sup>p</sup>	24.00	2.89 ± 2.44	1.81 ± 1.14	0.0141	0	SFG
3710	79	150.411854	2.074826	150.44456	2.054150	0.334	0.324 <sup>s</sup>	22.13	1.81 ± 0.86	1.73 ± 0.58	0.0417	6	SFG
3723	88	150.492909	2.068860	150.49783	2.069730	0.438	0.438 <sup>s</sup>	22.40	1.69 ± 0.81	1.61 ± 0.52	0.0299	4	AGN
3725	228	149.987745	2.585270	149.9898	2.587100	0.666	0.683 <sup>s</sup>	22.83	1.60 ± 1.13	1.46 ± 0.78	0.0199	0	SFG
3738	140	150.00754	2.274285	150.01012	2.273830	0.472	0.473 <sup>s</sup>	22.67	1.59 ± 1.07	1.53 ± 0.79	0.0268	3	SFG
3770	187	149.635991	2.403578	149.62376	2.399380	0.845	0.840 <sup>s</sup>	23.08	2.33 ± 1.60	1.86 ± 0.92	0.0231	38	AGN
3797	198	149.595659	2.440795	149.59607	2.437880	1.157	1.168 <sup>p</sup>	23.54	2.45 ± 1.87	1.81 ± 1.02	0.0182	0	SFG
3807	314	149.839731	2.130841	149.8505	2.142830	0.933	0.953 <sup>s</sup>	23.14	1.98 ± 1.40	1.59 ± 0.80	0.0174	3	SFG
3859	166	149.623273	2.321528	149.66098	2.315540	0.122	0.125 <sup>s</sup>	21.49	0.67 ± -0.05	1.06 ± 0.13	0.0561	0	SFG
3866	161	149.961433	2.349518	149.95676	2.347630	0.940	0.940 <sup>s</sup>	24.02	2.17 ± 1.41	1.72 ± 0.75	0.0194	3	AGN
3885	11	150.170849	1.690854	150.19728	1.658950	0.221	0.220 <sup>s</sup>	21.82	2.54 ± 0.75	2.23 ± 0.24	0.0838	9	SFG
3948	166	149.646187	2.290949	149.66098	2.315540	0.120	0.125 <sup>s</sup>	21.39	0.67 ± -0.05	1.06 ± 0.13	0.0561	1	SFG
4004	310	150.553243	2.486087	150.55296	2.499640	0.874	0.879 <sup>s</sup>	23.27	2.14 ± 1.69	1.73 ± 1.06	0.0203	8	SFG
4058	158	150.753455	2.361137	150.75114	2.354180	0.191	0.177 <sup>s</sup>	22.02	0.87 ± 0.36	1.17 ± 0.45	0.0450	9	SFG
4092	237	150.146065	2.698520	150.11756	2.692520	0.350	0.349 <sup>s</sup>	22.26	2.19 ± 0.95	1.96 ± 0.52	0.0468	3	SFG
4113	161	149.97009	2.335386	149.95676	2.347630	0.934	0.940 <sup>s</sup>	23.27	2.17 ± 1.41	1.72 ± 0.75	0.0194	0	SFG
4145	69	150.418126	1.976737	150.41965	1.973820	0.865	0.863 <sup>s</sup>	23.35	1.74 ± 1.49	1.47 ± 0.99	0.0170	4	SFG
4148	91	150.14614	2.064044	150.1452	2.044110	0.709	0.720 <sup>s</sup>	22.88	1.15 ± 0.85	1.29 ± 0.76	0.0273	6	SFG
4172	86	150.054373	1.999658	150.0123	2.034610	0.078	0.079 <sup>s</sup>	20.73	0.41 ± -0.23	0.91 ± 0.06	0.0758	73	SFG
4294	257	150.592235	2.873636	150.5883	2.864990	0.933	0.910 <sup>p</sup>	23.22	2.35 ± 1.73	1.85 ± 1.02	0.0219	2	AGN
4324	220	149.929322	2.518502	149.92079	2.521660	0.751	0.729 <sup>s</sup>	23.17	3.05 ± 1.49	2.37 ± 0.61	0.0376	88	AGN
4391	135	150.087847	2.194544	150.09421	2.198250	0.688	0.682 <sup>s</sup>	22.80	1.61 ± 1.08	1.46 ± 0.72	0.0196	1	AGN
4477	76	150.416308	2.012041	150.4221	2.007470	0.880	0.870 <sup>s</sup>	23.46	2.13 ± 1.50	1.73 ± 0.89	0.0208	0	SFG
4489	315	149.968632	2.583275	149.974781	2.562600	0.309	0.308 <sup>s</sup>	22.45	0.58 ± 0.34	0.95 ± 0.47	0.0238	3	SFG
4528	25	149.886865	1.769746	149.85402	1.770230	0.125	0.124 <sup>s</sup>	21.29	1.58 ± 0.08	1.65 ± -0.05	0.0884	8	SFG
4609	229	149.717893	2.539343	149.706564	2.551300	0.490	0.477 <sup>s</sup>	22.59	1.57 ± 0.85	1.52 ± 0.59	0.0263	2	SFG
4615	203	149.658219	2.475676	149.65762	2.479720	0.948	0.948 <sup>s</sup>	23.16	2.28 ± 1.59	1.78 ± 0.89	0.0201	1	SFG
4691	136	150.17598	2.215562	150.17749	2.215910	0.667	0.671 <sup>s</sup>	22.76	1.73 ± 1.10	1.54 ± 0.70	0.0210	2	SFG
4692	231	150.052284	2.594777	150.05621	2.590850	0.696	0.687 <sup>s</sup>	22.81	1.98 ± 1.73	1.70 ± 1.22	0.0238	30	SFG
4695	190	149.458268	2.437884	149.45692	2.433530	0.482	0.484 <sup>s</sup>	23.11	2.16 ± 1.36	1.89 ± 0.89	0.0347	44	SFG
4718	124	150.067527	2.23217	150.05408	2.204690	0.186	0.186 <sup>s</sup>	21.66	0.86 ± 0.08	1.17 ± 0.17	0.0427	2	SFG
4828	230	149.985521	2.554335	149.98592	2.564900	0.728	0.725 <sup>s</sup>	23.34	1.61 ± 1.13	1.45 ± 0.75	0.0186	8	SFG
4843	220	149.952535	2.516362	149.92079	2.521660	0.729	0.729 <sup>s</sup>	22.84	3.05 ± 1.49	2.37 ± 0.61	0.0376	23	SFG
4950	194	149.681691	2.412496	149.70296	2.400810	0.390	0.364 <sup>s</sup>	22.23	1.34 ± 0.80	1.41 ± 0.66	0.0304	12	SFG

Notes. (Continued)

Table A.1. Radio properties of Group Galaxies in COSMOS

ID	3 GHz		radio		X-ray		Redshift z		$\log_{10}(L_{1.4 \text{ GHz}} / \text{W Hz}^{-1})$	$\log_{10}(L_X / 10^{42} \text{ erg s}^{-1})$	$\log_{10}(M_{200c} / 10^{13} M_{\odot})$	$R_{200c}$ (deg.)	BGG Rank	Radio Class
	(1)	(2)	R.A. (3)	Dec. (deg., J2000.0) (4)	R.A. (5)	Dec. (6)	Radio (7)	X-ray (8)						
4962	76	150.425649	2.021020	150.4221	2.007470	0.860	0.870 <sup>s</sup>	23.36	2.13 ± 1.50	1.73 ± 0.89	0.0208	5	SFG	
4991	65	149.894388	1.947530	149.89253	1.944590	0.772	0.773 <sup>s</sup>	23.29	1.66 ± 1.27	1.46 ± 0.84	0.0181	4	SFG	
5007	304	150.405059	2.410020	150.41328	2.409970	0.374	0.385 <sup>s</sup>	22.38	1.89 ± 0.74	1.75 ± 0.41	0.0371	10	SFG	
5018	88	150.499727	2.077642	150.49783	2.069730	0.438	0.438 <sup>s</sup>	22.33	1.69 ± 0.81	1.61 ± 0.52	0.0299	15	AGN	
5039	220	149.903547	2.544502	149.92079	2.521660	0.728	0.729 <sup>s</sup>	22.82	3.05 ± 1.49	2.37 ± 0.61	0.0376	47	SFG	
5050	179	149.868044	2.351833	149.87582	2.345200	0.346	0.356 <sup>s</sup>	22.27	1.45 ± 0.66	1.48 ± 0.49	0.0318	6	SFG	
5156	145	149.805265	2.260918	149.82838	2.261260	0.377	0.379 <sup>s</sup>	22.15	1.31 ± 0.59	1.38 ± 0.46	0.0282	6	SFG	
5170	174	149.644133	2.359209	149.64665	2.347520	0.953	0.964 <sup>s</sup>	23.10	2.54 ± 1.74	1.95 ± 0.95	0.0230	2	SFG	
5185	149	150.403886	2.508868	150.42235	2.428000	0.124	0.124 <sup>s</sup>	21.13	1.81 ± 0.16	1.79 ± -0.06	0.0986	1	SFG	
5191	300	149.748017	2.253157	149.72829	2.234420	0.355	0.369 <sup>s</sup>	22.10	1.39 ± 0.77	1.44 ± 0.61	0.0293	1	SFG	
5268	86	150.000355	1.978580	150.0123	2.034610	0.080	0.079 <sup>s</sup>	20.88	0.41 ± -0.23	0.91 ± 0.06	0.0758	4	SFG	
5296	6	150.2938	1.555741	150.29951	1.553430	0.365	0.360 <sup>s</sup>	22.50	2.06 ± 1.01	1.87 ± 0.62	0.0425	14	SFG	
5331	158	150.752422	2.358512	150.75114	2.354180	0.175	0.177 <sup>s</sup>	21.48	0.87 ± 0.36	1.17 ± 0.45	0.0450	7	SFG	
5346	68	150.003913	1.969464	149.9996	1.973280	0.600	0.600 <sup>s</sup>	22.83	1.64 ± 1.06	1.51 ± 0.72	0.0223	0	AGN	
5364	196	150.282222	2.460167	150.28171	2.418500	0.123	0.123 <sup>s</sup>	21.99	0.65 ± -0.12	1.05 ± 0.07	0.0564	4	SFG	
5377	216	150.054825	2.658520	150.06644	2.644100	0.674	0.696 <sup>s</sup>	22.73	1.86 ± 1.25	1.62 ± 0.80	0.0219	3	SFG	
5428	20	150.294717	1.587610	150.32584	1.605100	0.230	0.227 <sup>s</sup>	22.22	1.13 ± 0.43	1.33 ± 0.42	0.0419	11	SFG	
5491	20	150.328279	1.583153	150.32584	1.605100	0.240	0.227 <sup>s</sup>	21.94	1.13 ± 0.43	1.33 ± 0.42	0.0419	9	SFG	
5549	220	149.944824	2.536326	149.92079	2.521660	0.730	0.729 <sup>s</sup>	22.80	3.05 ± 1.49	2.37 ± 0.61	0.0376	7	SFG	
5569	88	150.470486	2.070085	150.49783	2.069730	0.441	0.438 <sup>s</sup>	22.29	1.69 ± 0.81	1.61 ± 0.52	0.0299	10	SFG	
5607	349	150.279696	1.695615	150.29168	1.689350	0.525	0.527 <sup>s</sup>	22.48	1.90 ± 0.98	1.68 ± 0.55	0.0274	2	SFG	
5629	231	150.059482	2.594074	150.05621	2.590850	0.700	0.687 <sup>s</sup>	22.77	1.98 ± 1.73	1.70 ± 1.22	0.0238	21	SFG	
5688	371	149.627712	2.396169	149.61563	2.386330	0.117	0.125 <sup>s</sup>	21.21	0.73 ± -0.06	1.09 ± 0.09	0.0562	53	SFG	
5749	178	150.634371	2.383231	150.6369	2.384230	0.372	0.372 <sup>s</sup>	22.47	2.25 ± 1.71	1.74 ± 0.98	0.0186	0	AGN	
5750	394	149.810143	2.123724	149.81022	2.148230	0.354	0.354 <sup>s</sup>	22.05	1.52 ± 0.89	1.51 ± 0.67	0.0323	6	SFG	
5784	224	149.914751	2.601362	149.91911	2.600870	0.246	0.247 <sup>s</sup>	21.87	0.93 ± 0.29	1.19 ± 0.34	0.0341	6	SFG	
5841	149	150.346589	2.404179	150.42235	2.428000	0.127	0.124 <sup>s</sup>	21.44	1.81 ± 0.16	1.79 ± -0.06	0.0986	9	SFG	
5898	231	150.045479	2.578946	150.05621	2.590850	0.680	0.687 <sup>s</sup>	22.73	1.98 ± 1.73	1.70 ± 1.22	0.0238	16	SFG	
6029	394	149.800779	2.140348	149.81022	2.148230	0.355	0.354 <sup>s</sup>	22.54	1.52 ± 0.89	1.51 ± 0.67	0.0323	8	SFG	
6186	387	149.537096	2.721989	149.53951	2.718650	0.855	0.855 <sup>s</sup>	22.99	1.70 ± 1.23	1.42 ± 0.74	0.0165	0	SFG	
6190	392	150.598325	1.723302	150.6236	1.717600	0.378	0.366 <sup>s</sup>	22.11	1.16 ± 0.58	1.28 ± 0.49	0.0268	2	SFG	
6219	303	149.994211	2.257883	150.0087	2.260610	0.659	0.662 <sup>s</sup>	22.90	1.67 ± 1.34	1.51 ± 0.96	0.0208	0	AGN	
6235	271	149.911417	2.682767	149.91853	2.700660	0.863	0.890 <sup>s</sup>	22.91	2.33 ± 1.60	1.84 ± 0.90	0.0221	2	SFG	
6281	97	149.863797	2.058724	149.86475	2.063340	1.225	1.229 <sup>p</sup>	23.41	2.30 ± 1.71	1.70 ± 0.90	0.0165	2	SFG	
6290	220	149.918795	2.500697	149.92079	2.521660	0.753	0.729 <sup>s</sup>	22.76	3.05 ± 1.49	2.37 ± 0.61	0.0376	106	SFG	
6420	277	150.00463	2.632772	150.005	2.631360	0.677	0.677 <sup>s</sup>	22.68	1.55 ± 1.23	1.43 ± 0.88	0.0192	0	SFG	
6426	217	150.001894	2.460875	150.0037	2.454870	0.733	0.732 <sup>s</sup>	22.76	1.73 ± 1.15	1.52 ± 0.73	0.0196	12	SFG	
6432	304	150.407166	2.426007	150.41328	2.409970	0.386	0.385 <sup>s</sup>	22.10	1.89 ± 0.74	1.75 ± 0.41	0.0371	15	SFG	
6494	143	150.206265	2.285781	150.22014	2.278510	0.874	0.885 <sup>s</sup>	22.94	2.18 ± 1.43	1.75 ± 0.79	0.0207	14	SFG	
6544	20	150.338731	1.614247	150.32584	1.605100	0.226	0.227 <sup>s</sup>	21.64	1.13 ± 0.43	1.33 ± 0.42	0.0419	12	SFG	

Notes. (Continued)

Table A.1. Radio properties of Group Galaxies in COSMOS

ID	3 GHz		radio		X-ray		Redshift z		$\log_{10}(L_{1.4 \text{ GHz}} / \text{W Hz}^{-1})$	$\log_{10}(L_X / 10^{42} \text{ erg s}^{-1})$	$\log_{10}(M_{200c} / 10^{13} M_{\odot})$	$R_{200c}$ (deg.)	BGG Rank	Radio Class
	(1)	(2)	R.A. (3)	Dec. (deg., J2000.0) (4)	R.A. (5)	Dec. (6)	Radio (7)	X-ray (8)						
6567	11	150.203909	1.638906	150.19728	1.658950	0.217	0.220 <sup>s</sup>	21.56	2.54 ± 0.75	2.23 ± 0.24	0.0838	2	SFG	
6570	395	149.826096	2.135200	149.8261	2.135200	0.168	0.169 <sup>s</sup>	21.30	0.09 ± -0.10	0.67 ± 0.24	0.0314	0	SFG	
6674	199	150.708047	2.292326	150.70682	2.292530	1.099	1.095 <sup>s</sup>	23.46	2.01 ± 1.66	1.70 ± 1.13	0.0226	41	AGN	
6773	220	149.915143	2.506341	149.92079	2.521660	0.727	0.729 <sup>s</sup>	23.15	3.05 ± 1.49	2.37 ± 0.61	0.0376	29	SFG	
6869	359	150.66498	1.993717	150.68078	1.996200	0.430	0.438 <sup>s</sup>	22.22	1.34 ± 0.72	1.36 ± 0.53	0.0244	0	SFG	
6878	297	150.198436	2.068476	150.20406	2.067260	0.185	0.186 <sup>s</sup>	22.00	0.77 ± 0.36	1.11 ± 0.47	0.0409	44	SFG	
6980	271	149.90983	2.709281	149.91853	2.700660	0.892	0.890 <sup>s</sup>	22.92	2.33 ± 1.60	1.84 ± 0.90	0.0221	6	SFG	
6983	297	150.173711	2.060715	150.20406	2.067260	0.185	0.186 <sup>s</sup>	21.36	0.77 ± 0.36	1.11 ± 0.47	0.0409	0	SFG	
7008	374	150.774823	2.464773	150.77491	2.457450	0.979	0.979 <sup>s</sup>	23.10	2.22 ± 1.88	1.70 ± 1.13	0.0183	3	SFG	
7023	25	149.843865	1.777358	149.85402	1.770230	0.122	0.124 <sup>s</sup>	21.38	1.58 ± 0.08	1.65 ± -0.05	0.0884	3	SFG	
7059	239	150.106118	2.722754	150.10533	2.723920	0.734	0.731 <sup>s</sup>	23.29	1.87 ± 1.33	1.61 ± 0.85	0.0211	2	AGN	
7090	224	149.907977	2.608937	149.91911	2.600870	0.265	0.247 <sup>s</sup>	22.35	0.93 ± 0.29	1.19 ± 0.34	0.0341	1	SFG	
7168	220	149.914282	2.510761	149.92079	2.521660	0.726	0.729 <sup>s</sup>	22.94	3.05 ± 1.49	2.37 ± 0.61	0.0376	27	AGN	
7184	392	150.621974	1.710732	150.6236	1.717600	0.369	0.366 <sup>s</sup>	22.33	1.16 ± 0.58	1.28 ± 0.49	0.0268	3	SFG	
7220	365	149.478187	2.119795	149.48046	2.124930	0.125	0.126 <sup>s</sup>	21.54	0.79 ± 0.07	1.13 ± 0.20	0.0578	1	SFG	
7250	142	150.288047	2.276944	150.28607	2.278140	0.123	0.123 <sup>s</sup>	21.47	0.62 ± -0.21	1.03 ± -0.00	0.0559	1	SFG	
7254	191	150.072236	2.366258	150.11295	2.359490	0.218	0.220 <sup>s</sup>	21.52	1.15 ± 0.26	1.34 ± 0.24	0.0423	109	SFG	
7272	276	149.986045	2.685777	149.9862	2.684860	1.190	1.180 <sup>p</sup>	23.20	2.57 ± 1.89	1.89 ± 0.99	0.0192	0	SFG	
7283	220	149.914544	2.542401	149.92079	2.521660	0.729	0.729 <sup>s</sup>	22.69	3.05 ± 1.49	2.37 ± 0.61	0.0376	35	SFG	
7288	193	150.081866	2.415688	150.0918	2.393330	0.218	0.220 <sup>s</sup>	21.52	1.41 ± 0.29	1.51 ± 0.18	0.0481	63	SFG	
7292	74	149.821768	1.998937	149.82828	2.013430	0.695	0.696 <sup>s</sup>	22.66	1.89 ± 1.30	1.64 ± 0.83	0.0221	4	SFG	
7321	12	150.378375	1.542800	150.37868	1.538840	1.112	1.110 <sup>p</sup>	23.60	2.44 ± 1.98	1.82 ± 1.14	0.0186	0	SFG	
7356	262	149.590609	2.807043	149.59956	2.819910	0.343	0.342 <sup>s</sup>	22.23	2.24 ± 1.00	2.00 ± 0.55	0.0488	23	SFG	
7364	257	150.608791	2.859481	150.5883	2.864990	0.921	0.910 <sup>p</sup>	23.34	2.35 ± 1.73	1.85 ± 1.02	0.0219	0	SFG	
7379	40	150.41384	1.847586	150.4125	1.848880	0.972	0.973 <sup>s</sup>	23.47	2.49 ± 1.56	1.92 ± 0.78	0.0221	3	SFG	
7381	216	150.082066	2.657093	150.06644	2.644100	0.696	0.696 <sup>s</sup>	22.82	1.86 ± 1.25	1.62 ± 0.80	0.0219	2	SFG	
7415	317	150.122195	2.000182	150.12646	1.999260	1.059	1.019 <sup>p</sup>	23.11	2.11 ± 1.49	1.65 ± 0.82	0.0175	0	SFG	
7458	356	150.664108	1.861732	150.6687	1.875570	0.403	0.386 <sup>s</sup>	22.11	1.23 ± 0.62	1.31 ± 0.48	0.0249	0	SFG	
7481	130	150.016431	2.218702	150.02185	2.201720	0.940	0.941 <sup>s</sup>	22.97	2.34 ± 1.58	1.83 ± 0.86	0.0210	3	SFG	
7513	236	150.220708	2.740914	150.21767	2.737930	0.936	0.923 <sup>s</sup>	22.96	2.12 ± 1.51	1.69 ± 0.87	0.0190	4	SFG	
7555	313	149.736014	2.073886	149.73878	2.082480	0.525	0.533 <sup>s</sup>	22.55	2.17 ± 1.56	1.69 ± 0.87	0.0180	1	SFG	
7636	343	150.414564	2.774186	150.39865	2.762250	0.815	0.818 <sup>s</sup>	23.20	2.53 ± 1.73	2.00 ± 0.99	0.0263	14	SFG	
7662	97	149.87442	2.071398	149.86475	2.063340	1.230	1.229 <sup>p</sup>	23.22	2.30 ± 1.71	1.70 ± 0.90	0.0165	1	SFG	
7682	31	150.48519	1.803062	150.49237	1.794250	0.957	0.958 <sup>s</sup>	22.95	2.34 ± 1.63	1.82 ± 0.91	0.0207	4	SFG	
7762	403	150.003525	1.746226	150.00259	1.745640	1.826	1.800 <sup>p</sup>	23.83	2.59 ± 2.08	1.62 ± 0.89	0.0122	0	SFG	
7770	292	150.026788	2.562057	150.03386	2.551700	0.745	0.746 <sup>s</sup>	22.71	1.65 ± 1.34	1.46 ± 0.93	0.0185	1	SFG	
7802	114	150.606279	2.131423	150.59361	2.127080	0.698	0.727 <sup>s</sup>	22.63	2.01 ± 1.29	1.70 ± 0.77	0.0225	2	AGN	
7834	218	149.790468	2.466663	149.77321	2.463440	0.723	0.735 <sup>p</sup>	23.05	1.53 ± 1.20	1.39 ± 0.84	0.0177	3	SFG	
7887	109	150.224451	2.104840	150.22498	2.105740	0.786	0.751 <sup>p</sup>	22.76	2.16 ± 1.67	1.68 ± 0.97	0.0177	0	SFG	
7890	241	150.465416	2.746066	150.4879	2.751180	0.632	0.611 <sup>s</sup>	22.71	1.82 ± 1.21	1.62 ± 0.80	0.0240	8	SFG	

Notes. (Continued)

Table A.1. Radio properties of Group Galaxies in COSMOS

ID		radio				X-ray		Redshift $z$		$\log_{10}(L_{1.4} \text{ GHz} / \text{W Hz}^{-1})$	$\log_{10}(L_X / 10^{42} \text{ erg s}^{-1})$	$\log_{10}(M_{200c} / 10^{13} M_{\odot})$	$R_{200c}$ (deg.)	BGG Rank	Radio Class
3 GHz	X-ray	R.A.	Dec.	R.A.	Dec.	Radio	X-ray	(7)	(8)	(9)	(10)	(11)	(12)	(13)	(14)
(1)	(2)	(3)	(4)	(5)	(6)	(7)	(8)	(9)	(10)	(11)	(12)	(13)	(14)	(15)	(16)
7894	275	149.839301	2.693789	149.83842	2.675170	0.270	0.264 <sup>s</sup>	21.72	1.28 ± 0.82	1.41 ± 0.73	0.0388	2	SFG		
7920	243	150.259569	2.769150	150.26115	2.768570	1.308	1.315 <sup>p</sup>	23.27	2.52 ± 1.96	1.80 ± 1.03	0.0168	3	SFG		
7938	239	150.09445	2.734668	150.10533	2.723920	0.739	0.731 <sup>s</sup>	22.74	1.87 ± 1.33	1.61 ± 0.85	0.0211	5	SFG		
7964	11	150.202127	1.652779	150.19728	1.658950	0.220	0.220 <sup>s</sup>	21.51	2.54 ± 0.75	2.23 ± 0.24	0.0838	3	SFG		
8022	275	149.832516	2.703061	149.83842	2.675170	0.268	0.264 <sup>s</sup>	21.68	1.28 ± 0.82	1.41 ± 0.73	0.0388	5	SFG		
8210	150	149.988623	2.319459	149.98035	2.314270	0.931	0.933 <sup>s</sup>	22.90	2.35 ± 1.48	1.84 ± 0.76	0.0214	12	SFG		
8229	246	149.801327	2.931266	149.76143	2.926720	0.359	0.350 <sup>s</sup>	22.35	2.59 ± 1.52	2.21 ± 0.95	0.0568	7	SFG		
8266	171	149.662528	2.269566	149.675	2.274600	0.675	0.678 <sup>s</sup>	22.61	1.73 ± 1.30	1.54 ± 0.89	0.0210	1	SFG		
8297	224	149.919102	2.600931	149.91911	2.600870	0.248	0.247 <sup>s</sup>	21.77	0.93 ± 0.29	1.19 ± 0.34	0.0341	0	SFG		
8303	220	149.912531	2.527176	149.92079	2.521660	0.736	0.729 <sup>s</sup>	22.66	3.05 ± 1.49	2.37 ± 0.61	0.0376	124	SFG		
8308	398	150.537541	1.930658	150.544	1.922700	0.461	0.463 <sup>s</sup>	22.21	1.59 ± 0.80	1.51 ± 0.51	0.0263	1	SFG		
8374	93	149.654698	2.101979	149.66565	2.075670	0.340	0.339 <sup>s</sup>	21.99	1.54 ± 0.85	1.55 ± 0.65	0.0349	3	SFG		
8386	262	149.624552	2.852695	149.59956	2.819910	0.363	0.342 <sup>s</sup>	22.01	2.24 ± 1.00	2.00 ± 0.55	0.0488	45	SFG		
8488	250	149.94541	2.923600	149.94826	2.921580	0.125	0.126 <sup>p</sup>	21.19	1.51 ± 0.89	1.60 ± 0.77	0.0838	1	SFG		
8521	125	150.621441	2.158812	150.62251	2.160390	1.527	1.500 <sup>p</sup>	23.42	2.62 ± 2.26	1.81 ± 1.23	0.0161	15	SFG		
8547	172	149.938583	2.413817	149.93372	2.409940	0.842	0.874 <sup>p</sup>	23.19	1.94 ± 1.31	1.60 ± 0.76	0.0185	2	SFG		
8613	52	150.449503	1.882698	150.44759	1.883190	0.673	0.672 <sup>s</sup>	22.87	1.84 ± 1.17	1.62 ± 0.74	0.0223	9	SFG		
8632	365	149.492792	2.153128	149.48046	2.124930	0.126	0.126 <sup>s</sup>	21.07	0.79 ± 0.07	1.13 ± 0.20	0.0578	0	AGN		
8729	118	149.638144	2.149568	149.63382	2.136720	0.952	0.944 <sup>s</sup>	22.94	2.12 ± 1.55	1.68 ± 0.89	0.0186	5	SFG		
8756	220	149.920606	2.499627	149.92079	2.521660	0.731	0.729 <sup>s</sup>	22.63	3.05 ± 1.49	2.37 ± 0.61	0.0376	21	SFG		
8820	231	150.058541	2.602054	150.05621	2.590850	0.696	0.687 <sup>s</sup>	22.61	1.98 ± 1.73	1.70 ± 1.22	0.0238	9	SFG		
8825	268	150.540692	2.732980	150.53626	2.737500	0.345	0.349 <sup>s</sup>	22.13	0.85 ± 0.59	1.10 ± 0.61	0.0242	1	SFG		
8929	65	149.896908	1.946198	149.89253	1.944590	0.750	0.773 <sup>s</sup>	22.90	1.66 ± 1.27	1.46 ± 0.84	0.0181	2	SFG		
8982	21	150.15244	1.603324	150.14821	1.603690	0.333	0.345 <sup>p</sup>	21.95	1.72 ± 1.15	1.59 ± 0.81	0.0262	0	SFG		
9143	289	150.120109	2.561513	150.11438	2.555190	0.500	0.502 <sup>s</sup>	22.58	1.62 ± 0.96	1.54 ± 0.66	0.0258	6	SFG		
9157	220	149.926731	2.498903	149.92079	2.521660	0.728	0.729 <sup>s</sup>	22.64	3.05 ± 1.49	2.37 ± 0.61	0.0376	4	SFG		
9320	376	149.756214	2.735163	149.75333	2.733180	0.182	0.193 <sup>s</sup>	21.27	0.79 ± 0.24	1.11 ± 0.33	0.0378	24	SFG		
9324	145	149.82592	2.277071	149.82838	2.261260	0.380	0.379 <sup>s</sup>	22.28	1.31 ± 0.59	1.38 ± 0.46	0.0282	7	SFG		
9325	284	149.511969	2.633521	149.52184	2.617000	0.720	0.736 <sup>p</sup>	22.88	1.63 ± 1.15	1.52 ± 0.82	0.0229	1	AGN		
9368	305	149.641165	2.330826	149.6412	2.330890	0.502	0.502 <sup>s</sup>	22.27	1.41 ± 0.93	1.41 ± 0.70	0.0234	0	SFG		
9403	362	149.641098	2.061265	149.62906	2.066010	0.314	0.313 <sup>s</sup>	22.02	1.03 ± 0.49	1.21 ± 0.46	0.0284	3	SFG		
9411	324	150.019508	2.352622	150.02414	2.360500	0.726	0.726 <sup>s</sup>	22.88	1.49 ± 1.16	1.37 ± 0.81	0.0175	3	SFG		
9413	18	149.789805	1.624822	149.76518	1.623550	0.380	0.371 <sup>s</sup>	22.04	1.52 ± 1.04	1.52 ± 0.82	0.0320	5	SFG		
9489	333	150.022764	2.667363	150.04736	2.693170	0.220	0.219 <sup>s</sup>	21.74	1.03 ± 0.40	1.26 ± 0.43	0.0400	1	SFG		
9525	64	150.217418	1.978785	150.19821	1.985060	0.441	0.440 <sup>s</sup>	22.10	1.53 ± 0.74	1.51 ± 0.51	0.0278	6	SFG		
9539	35	150.230518	1.821048	150.2102	1.820140	0.525	0.529 <sup>s</sup>	22.55	1.85 ± 1.02	1.67 ± 0.64	0.0275	14	SFG		
9584	283	149.448797	2.564044	149.47871	2.561630	0.379	0.379 <sup>s</sup>	22.19	1.40 ± 0.81	1.45 ± 0.64	0.0301	2	SFG		
9649	283	149.485673	2.565090	149.47871	2.561630	0.384	0.379 <sup>s</sup>	22.13	1.40 ± 0.81	1.45 ± 0.64	0.0301	7	SFG		
9839	284	149.51049	2.625062	149.52184	2.617000	0.703	0.736 <sup>p</sup>	22.68	1.63 ± 1.15	1.52 ± 0.82	0.0229	0	SFG		
9844	79	150.448558	2.092895	150.4456	2.054150	0.329	0.324 <sup>s</sup>	22.04	1.81 ± 0.86	1.73 ± 0.58	0.0417	5	SFG		

Notes. (Continued)

Table A.1. Radio properties of Group Galaxies in COSMOS

3 GHz	X-ray		radio		X-ray		Redshift $z$		$\log_{10}(L_{1.4} \text{ GHz} / \text{W Hz}^{-1})$ (9)	$\log_{10}(L_X / 10^{42} \text{ erg s}^{-1})$ (10)	$\log_{10}(M_{200c} / 10^{13} M_{\odot})$ (11)	$R_{200c}$ (deg.) (12)	BGG Rank (13)	Radio Class (14)
	ID	(1)	(2)	R.A. (3)	Dec. (deg., J2000.0) (4)	R.A. (5)	Dec. (6)	Radio (7)						
9856	167	150.09321	2.320811	150.09583	2.299060	0.381	0.361 <sup>s</sup>	21.95	1.24 ± 0.56	1.35 ± 0.46	0.0286	15	SFG	
9953	11	150.206921	1.647137	150.19728	1.658950	0.218	0.220 <sup>s</sup>	21.45	2.54 ± 0.75	2.23 ± 0.24	0.0838	8	SFG	
9995	132	149.52106	2.168769	149.5124	2.182790	1.328	1.360 <sup>p</sup>	23.35	2.43 ± 1.93	1.80 ± 1.09	0.0182	1	SFG	
10044	192	150.139617	2.407064	150.1537	2.397640	0.901	0.897 <sup>s</sup>	22.82	2.00 ± 1.35	1.63 ± 0.77	0.0186	5	SFG	
10159	95	150.684252	2.066334	150.6741	2.085540	0.341	0.339 <sup>s</sup>	21.87	1.23 ± 0.70	1.35 ± 0.60	0.0298	2	SFG	
10167	281	150.085328	2.527423	150.08522	2.532770	0.876	0.889 <sup>s</sup>	22.80	2.37 ± 1.51	1.87 ± 0.80	0.0225	17	SFG	
10203	130	150.023799	2.203231	150.02185	2.201720	0.942	0.941 <sup>s</sup>	22.88	2.34 ± 1.58	1.83 ± 0.86	0.0210	0	SFG	
10239	234	150.161153	2.597904	150.16257	2.612660	0.890	0.892 <sup>s</sup>	22.83	2.03 ± 1.40	1.65 ± 0.81	0.0190	5	AGN	
10366	237	150.138599	2.702950	150.11756	2.692520	0.354	0.349 <sup>s</sup>	21.87	2.19 ± 0.95	1.96 ± 0.52	0.0468	43	SFG	
10433	52	150.453839	1.902745	150.44759	1.883190	0.664	0.672 <sup>s</sup>	22.48	1.84 ± 1.17	1.62 ± 0.74	0.0223	11	SFG	
10638	213	150.409498	2.505067	150.40456	2.516020	0.882	0.880 <sup>s</sup>	22.79	2.02 ± 1.33	1.64 ± 0.75	0.0190	12	SFG	
10831	226	150.396253	2.539676	150.40565	2.582670	0.114	0.107 <sup>s</sup>	20.81	0.51 ± -0.05	0.97 ± 0.19	0.0610	21	SFG	
10849	150	149.983285	2.323458	149.98035	2.314270	0.921	0.933 <sup>s</sup>	22.83	2.35 ± 1.48	1.84 ± 0.76	0.0214	20	SFG	
10877	192	150.158362	2.415354	150.1537	2.397640	0.899	0.897 <sup>s</sup>	22.82	2.00 ± 1.35	1.63 ± 0.77	0.0186	3	SFG	
10902	198	149.59713	2.441243	149.59607	2.437880	1.168	1.168 <sup>p</sup>	26.68	2.45 ± 1.87	1.81 ± 1.02	0.0182	7	AGN	
10905	379	150.624559	2.540305	150.61248	2.541790	0.432	0.432 <sup>s</sup>	24.55	1.72 ± 0.85	1.60 ± 0.53	0.0294	0	AGN	
10910	35	150.206627	1.823253	150.2102	1.820140	0.530	0.529 <sup>s</sup>	25.27	1.85 ± 1.02	1.67 ± 0.64	0.0275	0	AGN	
10912	138	149.508755	2.261351	149.50941	2.261110	0.943	0.937 <sup>s</sup>	24.57	2.53 ± 1.86	1.95 ± 1.07	0.0231	0	AGN	
10913	237	150.117854	2.684271	150.11756	2.692520	0.349	0.349 <sup>s</sup>	25.56	2.19 ± 0.95	1.96 ± 0.52	0.0468	164	AGN	
10918	262	149.600067	2.821154	149.59956	2.819910	0.345	0.342 <sup>s</sup>	25.36	2.24 ± 1.00	2.00 ± 0.55	0.0488	140	AGN	
10933	29	150.179959	1.768857	150.18167	1.770860	0.346	0.344 <sup>s</sup>	25.56	1.95 ± 0.72	1.81 ± 0.38	0.0422	0	AGN	
10936	347	150.117666	1.585710	150.11634	1.586110	0.839	0.839 <sup>s</sup>	26.10	1.96 ± 1.44	1.59 ± 0.86	0.0185	0	AGN	
10948	73	150.09076	1.999999	150.09186	1.999080	0.219	0.221 <sup>s</sup>	23.52	1.04 ± 0.19	1.27 ± 0.21	0.0397	0	AGN	
10950	250	149.95423	2.921232	149.94826	2.921580	0.126	0.126 <sup>p</sup>	22.99	1.51 ± 0.89	1.60 ± 0.77	0.0838	0	AGN	
10953	281	150.077103	2.548960	150.08522	2.532770	0.890	0.889 <sup>s</sup>	25.16	2.37 ± 1.51	1.87 ± 0.80	0.0225	2	AGN	
10956	191	150.114329	2.356473	150.11295	2.359490	0.220	0.220 <sup>s</sup>	24.00	1.15 ± 0.26	1.34 ± 0.24	0.0423	1	AGN	
10965	11	150.188705	1.646525	150.19728	1.658950	0.220	0.220 <sup>s</sup>	22.87	2.54 ± 0.75	2.23 ± 0.24	0.0838	4	SFG	
10966	6	150.278061	1.555656	150.29951	1.553430	0.361	0.360 <sup>s</sup>	24.18	2.06 ± 1.01	1.87 ± 0.62	0.0425	7	AGN	

Notes. (Continued)

**Table A.2.** Radio luminosity functions of group galaxies obtained with the  $V_{\max}$  method. A halo mass cut,  $M_{200c} > 10^{13.5} M_{\odot}$ , was applied. Note: the error on  $\Phi$  is in dex.

$z$	$z_{\text{med}}$	$\log L_{1.4 \text{ GHz}}$ [W Hz $^{-1}$ ]	$\log L_{1.4 \text{ GHz}}(\text{med})$ [W Hz $^{-1}$ ]	$\log \Phi$ [Mpc $^{-3}$ dex $^{-1}$ ]	N
0.07 – 0.4	0.345	21.268 – 22.000	21.524	$-4.073^{+0.198}_{-0.142}$	9
		22.000 – 22.891	22.488	$-4.292^{+0.084}_{-0.084}$	27
		22.891 – 23.781	23.025	$-4.979^{+0.259}_{-0.172}$	6
		23.781 – 24.671	24.420	$-5.470^{+0.573}_{-0.281}$	2
		24.671 – 25.587	25.459	$-5.181^{+0.343}_{-0.208}$	4
0.4 – 0.7	0.566	22.082 – 22.560	22.442	$-4.389^{+0.185}_{-0.135}$	10
		22.560 – 23.237	22.832	$-4.589^{+0.079}_{-0.079}$	31
		23.237 – 23.913	23.361	$-5.459^{+0.294}_{-0.188}$	5
		23.913 – 24.590	24.107	$-5.463^{+0.294}_{-0.188}$	5
		24.590 – 25.292	25.267	$-6.178^{+0.999}_{-0.359}$	1
0.7 – 1.0	0.881	22.605 – 22.920	22.791	$-4.118^{+0.109}_{-0.109}$	22
		22.920 – 23.715	23.298	$-4.678^{+0.061}_{-0.061}$	51
		23.715 – 24.510	24.056	$-5.254^{+0.109}_{-0.109}$	16
		24.510 – 25.304	24.566	$-5.983^{+0.422}_{-0.236}$	3
		25.304 – 26.125	26.099	$-6.475^{+0.999}_{-0.359}$	1
1.0 – 1.6	1.201	23.083 – 23.391	23.219	$-5.293^{+0.294}_{-0.188}$	5
		23.391 – 24.487	23.601	$-5.794^{+0.113}_{-0.113}$	15
		24.487 – 25.584	25.019	$-6.753^{+0.573}_{-0.281}$	2
		25.584 – 26.707	26.680	$-7.064^{+0.999}_{-0.359}$	1
1.6 – 2.3	1.987	23.746 – 24.159	24.049	$-6.082^{+0.343}_{-0.208}$	4

**Table A.3.** Radio luminosity functions of BGGs obtained with the  $V_{\max}$  method. A halo mass cut,  $M_{200c} > 10^{13.5} M_{\odot}$ , was applied. Note: the error on  $\Phi$  is in dex.

$z$	$z_{\text{med}}$	$\log L_{1.4 \text{ GHz}}$ [W Hz <sup>-1</sup> ]	$\log L_{1.4 \text{ GHz}}(\text{med})$ [W Hz <sup>-1</sup> ]	$\log \Phi$ [Mpc <sup>-3</sup> dex <sup>-1</sup> ]	N
0.07 – 0.4	0.346	21.926 – 22.000	21.948	$-4.506^{+0.999}_{-0.359}$	1
		22.000 – 22.889	22.522	$-5.051^{+0.294}_{-0.188}$	5
		22.889 – 23.779	23.159	$-5.270^{+0.422}_{-0.236}$	3
		23.779 – 24.668	24.361	$-5.771^{+0.999}_{-0.359}$	1
		24.668 – 25.583	25.557	$-5.783^{+0.999}_{-0.359}$	1
0.4 – 0.7	0.617	22.560 – 23.237	22.996	$-5.219^{+0.214}_{-0.150}$	8
		23.237 – 23.913	23.539	$-5.854^{+0.573}_{-0.281}$	2
		23.913 – 24.590	24.028	$-5.685^{+0.422}_{-0.236}$	3
		24.590 – 25.292	25.267	$-6.178^{+0.999}_{-0.359}$	1
0.7 – 1.0	0.894	22.656 – 22.920	22.761	$-4.911^{+0.422}_{-0.236}$	3
		22.920 – 23.715	23.338	$-5.316^{+0.121}_{-0.121}$	13
		23.715 – 24.510	24.095	$-5.506^{+0.198}_{-0.142}$	9
		24.510 – 25.304	24.566	$-6.461^{+0.999}_{-0.359}$	1
		25.304 – 26.125	26.099	$-6.475^{+0.999}_{-0.359}$	1
1.0 – 1.6	1.161	23.083 – 23.391	23.152	$-5.551^{+0.573}_{-0.281}$	2
		23.391 – 23.959	23.588	$-5.917^{+0.259}_{-0.172}$	6
		23.959 – 24.527	23.978	$-6.733^{+0.999}_{-0.359}$	1
		24.527 – 25.120	25.095	$-6.787^{+0.999}_{-0.359}$	1
1.6 – 2.3	1.987	23.746 – 24.159	24.049	$-6.082^{+0.343}_{-0.208}$	4

**Table A.4.** Radio luminosity functions of satellites obtained with the  $V_{\max}$  method. A halo mass cut,  $M_{200c} > 10^{13.5} M_{\odot}$ , was applied. Note: the error on  $\Phi$  is in dex.

$z$	$z_{\text{med}}$	$\log L_{1.4 \text{ GHz}}$ [W Hz $^{-1}$ ]	$\log L_{1.4 \text{ GHz}}(\text{med})$ [W Hz $^{-1}$ ]	$\log \Phi$ [Mpc $^{-3}$ dex $^{-1}$ ]	N
0.07 – 0.4	0.345	21.268 – 22.000	21.522	$-4.090^{+0.214}_{-0.150}$	8
		22.000 – 22.891	22.432	$-4.375^{+0.093}_{-0.093}$	22
		22.891 – 23.781	22.933	$-5.289^{+0.422}_{-0.236}$	3
		23.781 – 24.671	24.478	$-5.771^{+0.999}_{-0.359}$	1
		24.671 – 25.587	25.360	$-5.306^{+0.422}_{-0.236}$	3
0.4 – 0.7	0.530	22.082 – 22.560	22.442	$-4.389^{+0.185}_{-0.135}$	10
		22.560 – 22.956	22.706	$-4.586^{+0.106}_{-0.106}$	17
		22.956 – 23.351	23.093	$-5.045^{+0.234}_{-0.160}$	7
		23.351 – 23.747	23.371	$-5.625^{+0.573}_{-0.281}$	2
		23.747 – 24.167	24.125	$-5.654^{+0.573}_{-0.281}$	2
0.7 – 1.0	0.873	22.605 – 22.920	22.796	$-4.181^{+0.119}_{-0.119}$	19
		22.920 – 23.480	23.191	$-4.683^{+0.075}_{-0.075}$	34
		23.480 – 24.040	23.720	$-5.378^{+0.214}_{-0.150}$	8
		24.040 – 24.600	24.391	$-5.707^{+0.343}_{-0.208}$	4
		24.600 – 25.185	25.160	$-6.327^{+0.999}_{-0.359}$	1
1.0 – 1.6	1.230	23.196 – 23.391	23.266	$-5.443^{+0.422}_{-0.236}$	3
		23.391 – 24.213	23.521	$-5.929^{+0.214}_{-0.150}$	8
		24.213 – 25.035	24.943	$-6.929^{+0.999}_{-0.359}$	1
		25.858 – 26.707	26.680	$-6.942^{+0.999}_{-0.359}$	1

**Table A.5.** Best power law fit parameters. A halo mass cut,  $M_{200c} > 10^{13.5} M_{\odot}$ , was applied.

sample	$z$	$\log \Phi^*$ [Mpc $^{-3}$ dex $^{-1}$ ]	$\gamma$	$\log \Phi^*$ ( $\gamma = -0.75$ ) [Mpc $^{-3}$ dex $^{-1}$ ]
GGs	0.07-0.40	$-5.289^{+0.079}_{-0.089}$	$-0.518^{+0.054}_{-0.053}$	$-5.710^{+0.036}_{-0.040}$
GGs	0.40-0.70	$-5.975^{+0.116}_{-0.122}$	$-1.090^{+0.103}_{-0.104}$	$-5.649^{+0.033}_{0.037}$
GGs	0.70-1.0	$-5.323^{+0.038}_{-0.042}$	$-0.953^{+0.054}_{-0.057}$	$-5.231^{+0.023}_{-0.025}$
GGs	1.0-1.6	$-6.089^{+0.074}_{-0.130}$	$-0.777^{+0.148}_{-0.300}$	$-6.063^{+0.044}_{-0.049}$
GGs	1.6-2.3	$-6.044^{+0.113}_{-0.142}$	$-1.503^{+1.056}_{-1.008}$	$-6.083^{+0.109}_{-0.151}$
BGGs	0.07-0.40	$-5.613^{+0.125}_{-0.212}$	$-0.378^{+0.108}_{-0.158}$	$-6.101^{+0.068}_{-0.083}$
BGGs	0.40-0.70	$-5.978^{+0.162}_{-0.290}$	$-0.657^{+0.255}_{-0.357}$	$-6.027^{+0.060}_{-0.066}$
BGGs	0.70-1.0	$-5.785^{+0.058}_{-0.067}$	$-0.716^{+0.081}_{-0.092}$	$-5.796^{+0.043}_{-0.048}$
BGGs	1.0-1.6	$-6.611^{+0.121}_{-0.158}$	$-1.301^{+0.256}_{-0.257}$	$-6.453^{+0.076}_{-0.101}$
BGGs	1.6-2.3	$-6.034^{+0.113}_{-0.148}$	$-1.447^{+0.970}_{-1.042}$	$6.083^{+0.110}_{-0.159}$
SGs	0.07-0.40	$-5.825^{+0.121}_{-0.124}$	$-0.729^{+0.071}_{-0.069}$	$-5.853^{+0.042}_{-0.048}$
SGs	0.40-0.70	$-6.218^{+0.147}_{-0.169}$	$-1.220^{+0.123}_{-0.135}$	$-5.744^{+0.038}_{-0.045}$
SGs	0.70-1.0	$-5.625^{+0.081}_{-0.093}$	$-1.161^{+0.101}_{-0.109}$	$-5.381^{+0.028}_{-0.030}$
SGs	1.0-1.6	$-6.547^{+0.278}_{-0.470}$	$-1.316^{+0.571}_{-0.871}$	$-6.259^{+0.061}_{-0.069}$
High-mass groups	0.07-0.40	$-5.294^{+0.081}_{-0.088}$	$-0.521^{+0.053}_{-0.052}$	$-5.713^{+0.037}_{-0.042}$
High-mass groups	0.40-0.70	$-5.977^{+0.115}_{-0.116}$	$-1.092^{+0.102}_{-0.099}$	$-5.652^{+0.033}_{-0.024}$
High-mass groups	0.70-1.0	$-5.325^{+0.040}_{-0.045}$	$-0.958^{+0.054}_{-0.057}$	$-5.230^{+0.023}_{-0.024}$
High-mass groups	1.0-1.6	$-6.097^{+0.074}_{-0.138}$	$-0.797^{+0.160}_{-0.310}$	$-6.066^{+0.047}_{-0.051}$
High-mass groups	1.6-2.3	$-6.034^{+0.109}_{-0.153}$	$-1.445^{+1.002}_{-1.057}$	$-6.077^{+0.109}_{0.138}$
Low-mass groups	0.07-0.40	$-5.639^{+0.098}_{-0.111}$	$-0.880^{+0.059}_{-0.062}$	$-5.440^{+0.029}_{-0.030}$
Low-mass groups	0.40-0.70	$-6.008^{+0.141}_{-0.206}$	$-0.603^{+0.138}_{-0.167}$	$-6.168^{+0.069}_{-0.077}$
Low-mass groups	0.70-1.0	$-6.153^{+0.253}_{-0.381}$	$-0.988^{+0.307}_{-0.391}$	$-5.948^{+0.071}_{-0.084}$

**Table A.6.**  $\Phi^*$  fits using the scaled method. A halo mass cut,  $M_{200c} > 10^{13.5} M_{\odot}$ , was applied.

sample	$z$	$\log \Phi^*$ (scaled) [ $\text{Mpc}^{-3} \text{dex}^{-1}$ ]
GGs	0.07-0.40	$-6.132^{+0.038}_{-0.038}$
GGs	0.40-0.70	$-6.022^{+0.032}_{-0.035}$
GGs	0.70-1.0	$-5.546^{+0.024}_{-0.023}$
GGs	1.0-1.6	$-6.314^{+0.046}_{-0.048}$
GGs	1.6-2.3	$-6.012^{+0.112}_{-0.112}$
BGGs	0.07-0.40	$-6.630^{+0.079}_{-0.077}$
BGGs	0.40-0.70	$-6.400^{+0.066}_{-0.067}$
BGGs	0.70-1.0	$-6.199^{+0.053}_{-0.052}$
BGGs	1.0-1.6	$-6.572^{+0.076}_{-0.073}$
BGGs	1.6-2.3	$-6.004^{+0.106}_{-0.108}$
SGs	0.07-0.40	$-6.255^{+0.043}_{-0.043}$
SGs	0.40-0.70	$-6.096^{+0.039}_{-0.039}$
SGs	0.70-1.0	$-5.681^{+0.029}_{-0.029}$
SGs	1.0-1.6	$-6.555^{+0.068}_{-0.065}$
High-mass groups	0.07-0.40	$-6.132^{+0.038}_{-0.038}$
High-mass groups	0.40-0.70	$-6.021^{+0.034}_{-0.033}$
High-mass groups	0.70-1.0	$-5.546^{+0.024}_{-0.024}$
High-mass groups	1.0-1.6	$-6.317^{+0.049}_{-0.049}$
High-mass groups	1.6-2.3	$-6.010^{+0.116}_{-0.109}$
Low-mass groups	0.07-0.40	$-5.892^{+0.033}_{-0.029}$
Low-mass groups	0.40-0.70	$-6.746^{+0.073}_{-0.077}$
Low-mass groups	0.70-1.0	$-6.283^{+0.076}_{-0.073}$

**Table A.7.** Radio luminosity functions of AGN inside X-ray galaxy groups obtained with the  $V_{\max}$  method. A halo mass cut,  $M_{200c} > 10^{13.5} M_{\odot}$ , was applied. Note: the error on  $\Phi$  is in dex.

$z$	$z_{\text{med}}$	$\log L_{1.4 \text{ GHz}}$ [W Hz <sup>-1</sup> ]	$\log L_{1.4 \text{ GHz}}(\text{med})$ [W Hz <sup>-1</sup> ]	$\log \Phi$ [Mpc <sup>-3</sup> dex <sup>-1</sup> ]	N
0.07 – 0.4	0.344	22.820 – 23.607	23.089	-4.878 <sup>+0.108</sup> <sub>-0.108</sub>	16
		23.607 – 24.393	24.000	-5.440 <sup>+0.343</sup> <sub>-0.207</sub>	4
		24.393 – 25.179	24.827	-5.157 <sup>+0.572</sup> <sub>-0.280</sub>	2
		25.179 – 25.966	25.828	-5.422 <sup>+0.343</sup> <sub>-0.207</sub>	4
0.4 – 0.7	0.599	22.918 – 23.587	23.241	-5.992 <sup>+0.233</sup> <sub>-0.160</sub>	7
		23.587 – 24.257	23.755	-5.696 <sup>+0.198</sup> <sub>-0.142</sub>	9
		24.257 – 24.926	24.491	-5.817 <sup>+0.259</sup> <sub>-0.172</sub>	6
		24.926 – 25.596	25.070	-6.161 <sup>+0.343</sup> <sub>-0.207</sub>	4
0.7 – 1.0	0.880	23.493 – 24.204	23.867	-6.069 <sup>+0.566</sup> <sub>-0.365</sub>	19
		24.204 – 24.916	24.511	-6.077 <sup>+0.102</sup> <sub>-0.102</sub>	18
		24.916 – 25.628	25.342	-6.368 <sup>+0.233</sup> <sub>-0.160</sub>	7
		25.628 – 26.340	26.340	-8.998 <sup>+0.999</sup> <sub>-0.359</sub>	1
1.0 – 1.6	1.159	24.155 – 24.961	24.565	-7.352 <sup>+0.259</sup> <sub>-0.172</sub>	6
		24.961 – 25.767	25.457	-7.549 <sup>+0.422</sup> <sub>-0.236</sub>	3
		26.573 – 27.379	27.379	-9.823 <sup>+0.999</sup> <sub>-0.359</sub>	1

**Table A.8.** Radio luminosity functions of SFGs inside X-ray galaxy groups obtained with the  $V_{\max}$  method. A halo mass cut,  $M_{200c} > 10^{13.5} M_{\odot}$ , was applied. Note: the error on  $\Phi$  is in dex.

$z$	$z_{\text{med}}$	$\log L_{1.4 \text{ GHz}}$ [W Hz $^{-1}$ ]	$\log L_{1.4 \text{ GHz}}(\text{med})$ [W Hz $^{-1}$ ]	$\log \Phi$ [Mpc $^{-3}$ dex $^{-1}$ ]	N
0.07 – 0.4	0.339	21.654 – 22.354	21.992	-4.784 $^{+0.125}_{-0.125}$	12
		22.354 – 23.055	22.694	-4.594 $^{+0.092}_{-0.092}$	22
		23.055 – 23.756	23.232	-4.740 $^{+0.198}_{-0.142}$	9
		23.756 – 24.456	24.202	-4.800 $^{+0.572}_{-0.280}$	2
0.4 – 0.7	0.611	22.697 – 23.262	23.147	-5.647 $^{+0.120}_{-0.120}$	13
		23.262 – 23.828	23.441	-5.358 $^{+0.105}_{-0.105}$	17
		23.828 – 24.393	24.044	-5.312 $^{+0.572}_{-0.280}$	2
		24.393 – 24.959	24.959	-8.282 $^{+0.999}_{-0.359}$	1
0.7 – 1.0	0.879	23.268 – 23.709	23.457	-5.607 $^{+0.083}_{-0.083}$	27
		23.709 – 24.150	23.842	-5.639 $^{+0.094}_{-0.094}$	21
		24.150 – 24.592	24.244	-5.391 $^{+0.233}_{-0.160}$	7
		24.592 – 25.033	25.033	-7.879 $^{+0.999}_{-0.359}$	1
1.0 – 1.6	1.230	23.792 – 24.116	24.023	-6.954 $^{+0.669}_{-0.326}$	8
		24.116 – 24.441	24.292	-6.752 $^{+0.233}_{-0.160}$	7
		24.441 – 24.765	24.695	-7.016 $^{+0.422}_{-0.236}$	3
		24.765 – 25.090	25.090	-9.541 $^{+0.999}_{-0.359}$	1
1.6 – 2.3	1.987	24.602 – 24.767	24.684	-7.742 $^{+0.572}_{-0.280}$	2
		24.767 – 24.931	24.914	-7.031 $^{+0.572}_{-0.280}$	2

**Table A.9.**  $\chi^2$  test results for the GGs (Sec. 3.3.3), and AGN and SFGs (Sec. 5). PL is for the power law, linear regression fit and SC for the scaled fit. DoF denotes the degrees of freedom.

$z_{\text{bin}}$	model	GGs			AGN			SFGs		
		$\chi^2$	$p$ -value	DoF	$\chi^2$	$p$ -value	DoF	$\chi^2$	$p$ -value	DoF
1	PL	49.39	4e-10	4	11.54	0.009	3	4.37	0.224	3
1	SC	72.74	5e-15	4	9.24	0.026	3	7.96	0.047	3
2	PL	9.87	0.043	4	3.74	0.291	3	6.25	0.100	3
2	SC	13.05	0.011	4	8.15	0.043	3	5.96	0.114	3
3	PL	6.22	0.183	4	9.65	0.022	3	8.16	0.043	3
3	SC	16.07	0.003	4	10.85	0.013	3	6.87	0.076	3
4	PL	7.51	0.057	3	5.11	0.078	2	12.57	0.006	3
4	SC	24.12	2e-5	3	5.33	0.070	2	9.15	0.027	3
5	PL	0.00	–	0	–	–	–	3.37	0.066	1
5	SC	0.00	–	0	–	–	–	1.86	0.172	1